Spontaneous imbibition of a wetting film wrapping a cylinder corner

Si Suo[1]

[1]Royal Institute of Technology

November 8, 2023

Abstract

Spontaneous imbibition flows within confined geometries are commonly encountered in both natural phenomena and industrial applications. A profound knowledge of the underlying flow dynamics benefits a broad spectrum of engineering practices. Nonetheless, within this area, especially concerning complex geometries, there exists a substantial research gap. This work centers on the cylinder-plane geometry, employing a combined theoretical and numerical approach to investigate the process of a wetting film wrapping a cylinder corner. It is found that the advance of the liquid front generally follows the Lucas-Washburn kinetics, i.e., $\thalf$ scaling, but it also depends on the dynamics of the liquid source. Furthermore, we provide a theoretical estimation of the timescale associated with the imbibition process. Notably, this timescale is highly dependent on the wettability condition and the properties of the involved liquid. Importantly, the practicability of our theoretical framework is well confirmed by the numerical experiments.

Spontaneous imbibition of a wetting film wrapping a cylinder corner

Si Suo[1]

[1]Linné Flow Centre, KTH Royal Institute of Technology, Department of Engineering Mechanics, 10044 Stockholm, Sweden.

Key Points:

- A combined theoretical and numerical approach is employed to investigate the imbibition dynamics of wetting film wrapping a cylinder corner.
- The advance of liquid front generally follows the Lucas-Washburn kinetics but also depends on the boundary dynamics.
- A theoretical estimation of time lengths is provided in which wettability and liquid properties are well considered.

Corresponding author: Si Suo, `ssuo@kth.se`

Abstract

Spontaneous imbibition flows within confined geometries are commonly encountered in both natural phenomena and industrial applications. A profound knowledge of the underlying flow dynamics benefits a broad spectrum of engineering practices. Nonetheless, within this area, especially concerning complex geometries, there exists a substantial research gap. This work centers on the cylinder-plane geometry, employing a combined theoretical and numerical approach to investigate the process of a wetting film wrapping a cylinder corner. It is found that the advance of the liquid front generally follows the Lucas-Washburn kinetics, i.e., $t^{1/2}$ scaling, but it also depends on the dynamics of the liquid source. Furthermore, we provide a theoretical estimation of the timescale associated with the imbibition process. Notably, this timescale is highly dependent on the wettability condition and the properties of the involved liquid. Importantly, the practicability of our theoretical framework is well confirmed by the numerical experiments.

1 Introduction

Spontaneous imbibition flows, i.e, liquids driven by capillary pressure to wet confined geometries, such as capillary tubes (Cai et al., 2021), grooves (Tang & Tang, 1994; Deng et al., 2014), porous media (Suo et al., 2019; Ha et al., 2018), etc., serves a crucial role in various natural and industrial processes. The pioneering research dates back to the Lucas-Washburn equation (Washburn, 1921), which leads to a scaling law regarding the evolution of the liquid front $h(t)$ in capillaries, i.e., $h = Ct^{1/2}$. This type of scaling law describes a energy balance between the capillary and viscous terms. Specifically, the wetting liquid is driven by the capillary force to spread on the surface and tends to maximize the coverage over the surface, during which the interfacial energy decreases and is consumed by the viscous friction. When the gravity is considered, part of releasing interfacial energy is transformed to the gravity potential leading to a different $t^{1/3}$ scaling. Nevertheless, the Lucas-Washburn equation was developed for circular capillaries. Once the confined geometry is complex, to what extent the $t^{1/2}$ scaling can predict the imbibition dynamics and how to estimate the scaling coefficient C remains unexplored, especially when sharp corners come up in a geometry.

There have been certain works appealing to imbibition in corners. For a open V-shape groove, Tang and Tang (1994) theoretically proved that the imbibition dynamics follow the scaling $t^{1/2}$ ignoring the gravity or $t^{1/3}$ considering the gravity; Higuera et al. (2008) derived the same scaling law within the framework of the lubrication approximation. These scaling laws have been verified against the experimental observations (Higuera et al., 2008; Rye et al., 1996; Deng et al., 2014). Very recently, Zhou and Doi (2020) developed a theory model for corners with curved walls using the Onsager principle. Surprisingly, they found the above scaling law still works while the scaling coefficient C slightly depends on the wall shape. In a closed medium, like a square or rectangular tube, if the contact angle $\theta < 45°$, i.e., the Concus-Finn condition is satisfied (Concus & Finn, 1969), the liquid can wet the interior corners and forms "finger-like" films along the corners. The imbibition flows thus become manifold, i.e., the bulk flow and corner flows, and the synergistic effect of the corner and bulk flow should be carefully considered (Weislogel, 2012). Imbibition in square tubes have been numerically and theoretically investigated (Yu et al., 2018; J. Zhao et al., 2021; Gurumurthy et al., 2018). It is found that both flows follow the Lucas-Washburn kinetics and their coupling plays an evident role.

What's more complex, in a porous medium, especially a natural one, the inter-connected angular channels randomly distribute in its solid space, where corner flows are enhanced and bulk-corner flows are expected to interplay in a more complicated manner. Cylinder-based geometries are commonly used as a surrogate model of real porous media. A quantity of experimental and numerical works have been reported based on this geometrical

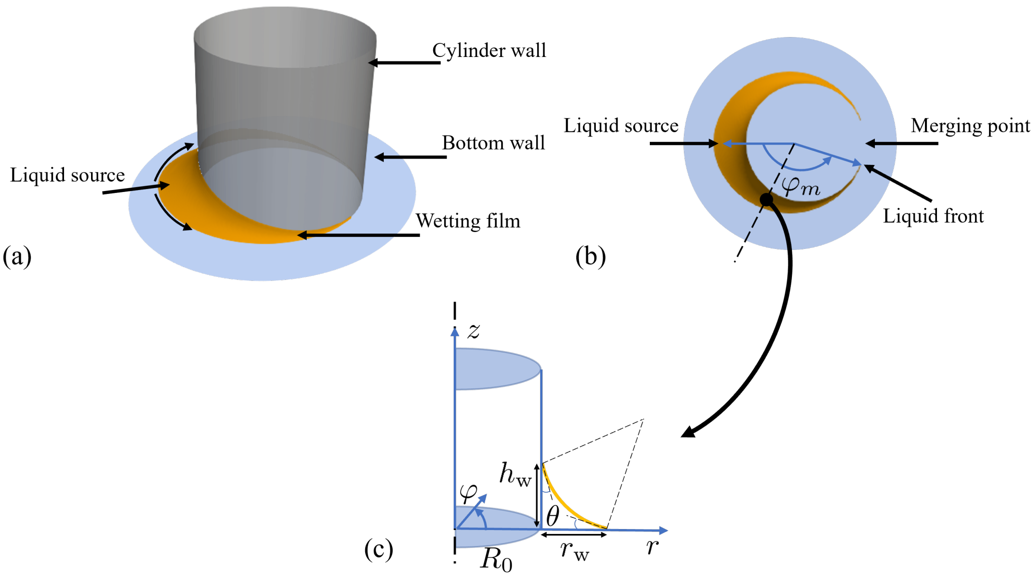

Figure 1. Schematics of the theoretical model, including a perspective view (a), a top view (b) and a sectional profile on the r-z plane of a cylindrical coordinate (c).

settings. B. Zhao et al. (2016) conducted a microfluidic experiment and directly visualized the process of liquid film spreading among cylinder corners in the strong imbibition regime ($\theta < 30°$). Numerical modelling works on corner flows in cylinder-based porous media are ensued (Primkulov et al., 2021; B. Zhao et al., 2019; Cox et al., 2023; Hu et al., 2018), and the corner flow is regarded as a specific flui-fluid diplacement pattern and emerges under certain combining conditions of capillary number, viscosity ratio and wettability.

Though a great progress regarding spontaneous imbibition flows within complex geometries has been made, answers to the fundamental questions posted in the beginning are still demanding because they are step stones towards better engineering practices. In this work, we shall focus on the cylinder-plane geometry and investigate the process of a liquid film wrapping a cylinder theoretically and numerically.

2 Theoretical model

We consider a film-cylinder system, as shown in figure 1(a). In this setting, a wetting film symmetrically spreads along the cylinder-bottom corner from a liquid source and finally merges at the other end. For describing this problem, a cylindrical coordinate (r-φ-z) is set up, where the liquid source locates at $\varphi = 0$ while the liquid front at $\varphi = \varphi_\mathrm{m}$, as can be seen in figure 1(b). Here, we assume that the characteristic size of the liquid film is smaller than the capillary length $l_c = \sqrt{\gamma/\rho g}$, where ρg is the liquid gravity and γ is the surface tension, so that the effect of gravity can be neglected. Additionally, we assume that the liquid-gas interface on the z-r plane is an arc, as shown in figure 1(c). Thus, the wetting height h_w and width r_w are equal. Provided the wettability condition θ and wetting width r_w, the film thickness h as a function of r is expressed as

$$h = R\cos\theta - \sqrt{R^2 - (r - R\cos\theta - R_0)}, \tag{1}$$

where R_0 is the cylinder radius and $R = r_\mathrm{w}/(\cos\theta - \sin\theta)$.

2.1 Time evolution equation

Using the Onsager principle, we derive the time evolution equation for the meniscus profile, which can be characterized by $r_{\mathrm{w}}(\varphi,t)$ for a given θ as per Eq. 1. For the present problem, it is stated in this principle that the dynamics of the system can be directly determined by the minimum of the Rayleighian (Doi, 2013),

$$\mathscr{R}\left[\dot{r}_{\mathrm{w}}(\varphi,t)\right]=\dot{F}\left[\dot{r}_{\mathrm{w}}(\varphi,t)\right]+\Phi\left[\dot{r}_{\mathrm{w}}(\varphi,t)\right], \tag{2}$$

where $\dot{F}$ is the change rate of the free energy of the film-cylinder system; and Φ is the energy dissipation function.

2.1.1 The change rate of free energy

The free energy of the system is a superposition of the interfacial energies along the liquid-cylinder wetting area $A_{ls1}(r_{\mathrm{w}})$, the liquid-wall wetting area $A_{ls2}(r_{\mathrm{w}})$ and the liquid-gas area $A_{lg}(r_{\mathrm{w}})$, and is given by

$$F=\gamma\left(-A_{ls1}\cos\theta-A_{ls2}\cos\theta+A_{lg}\right), \tag{3}$$

where

$$A_{ls1}(r_{\mathrm{w}}) = \int_0^{\varphi_{\mathrm{m}}} h_{\mathrm{w}} R_0\, d\varphi, \tag{4}$$

$$A_{ls2}(r_{\mathrm{w}}) = \int_0^{\varphi_{\mathrm{m}}}\int_{R_0}^{R_0+r_{\mathrm{w}}} r\, dr\, d\varphi, \tag{5}$$

$$A_{lg}(r_{\mathrm{w}}) = \int_0^{\varphi_{\mathrm{m}}}\int_{R_0}^{R_0+r_{\mathrm{w}}} \sqrt{h_r^2+h_\varphi^2/r^2+1}\, r\, dr\, d\varphi, \tag{6}$$

and h_r and h_φ are the derivatives of h concerning r and φ, respectively. The change rate of the free energy $\dot{F}$ is thus obtained as

$$\dot{F}=\gamma\dot{r}_{\mathrm{w}}\left(-A'_{ls1}\cos\theta-A'_{ls2}\cos\theta+A'_{lg}\right). \tag{7}$$

Here the top dot denotes the time derivative and the prime denotes the derivative with respect to r_{w}. Separately, A'_{ls1} and A'_{ls2} can be directly derived as

$$A'_{ls1} = \int_0^{\varphi_{\mathrm{m}}} R_0\, d\varphi, \tag{8}$$

$$A'_{ls2} = \int_0^{\varphi_{\mathrm{m}}} R_0 + r_{\mathrm{w}}\, d\varphi. \tag{9}$$

$$\tag{10}$$

As for A'_{lg}, since the size film is much thinner than the cylinder radius, i.e., $h \ll R_0$, and moreover $h_\varphi^2/r^2 \ll h_r^2 \ll 1$, A'_{lg} can be given as a simplified form

$$A'_{lg}=\int_0^{\varphi_{\mathrm{m}}}\left[(R_0+r_{\mathrm{w}})+\int_{R_0}^{R_0+r_{\mathrm{w}}} r h_r h'_r\, dr\right] d\varphi. \tag{11}$$

An auxiliary variable $a'(r_{\mathrm{w}})$ is defined as an integrated parts of F for the convenience of following usages, i.e.,

$$a'(r_{\mathrm{w}})=-(2R_0+r_{\mathrm{w}})\cos\theta+(R_0+r_{\mathrm{w}})+\int_{R_0}^{R_0+r_{\mathrm{w}}} r h_r h'_r\, dr. \tag{12}$$

We take the volume flux $Q(\varphi,t)$ of liquid flowing across the cross-section area, showing in figure 1 at φ, as an independent variable. Here, $Q(\varphi,t)$ is related to $\dot{r}_{\mathrm{w}}(\varphi,t)$ by the conservation equation, which reads

$$\frac{\partial A_l}{\partial t}=A'_l\dot{r}_{\mathrm{w}}=-\frac{1}{R_0}\frac{\partial Q}{\partial\varphi}, \tag{13}$$

where $A_l = \int_{R_0}^{R_0+r_\mathrm{w}} h\, dr$ is the cross-sectional area. Using the conservation equation Eq. 13, we can rewrite the change rate of free energy as a function of Q instead of $\dot{r}_\mathrm{w}$,

$$\dot{F} = \frac{\gamma}{R_0} \int_0^{\varphi_\mathrm{m}} \frac{\partial a'/A'_l}{\partial \varphi} Q\, d\varphi. \tag{14}$$

The definition of $\dot{F}$ as Eq. 14 suggests that $\dot{F}$ is a measurement of the power of capillary force. Thus, the capillary pressure P_c of the film-cylinder system can be estimated as

$$P_\mathrm{c} = \frac{\gamma}{R_0} \int_0^{\varphi_\mathrm{m}} \frac{\partial a'/A'_l}{\partial \varphi}\, d\varphi. \tag{15}$$

85 #### *2.1.2 Dissipation function*

Assuming that the liquid imbibes slowly along a cylinder corner, the inertia effect can be neglected. The flow is almost one-dimensional since u_φ is much larger than the u_r and u_z. Thus, flow dynamics can be described by the following Stokes equation

$$\eta \nabla^2 u_\varphi = \frac{\partial P}{R_0 \partial \varphi}, \tag{16}$$

where $\partial P/(R_0\partial\varphi)$ is the pressure gradient along the φ-axis. Provided $\partial P/(R_0\partial\varphi)$, Eq.16 is solved on the domain shown in figure 1 with no-slip boundary conditions, i.e., $u_\varphi = 0$ at the solid walls and shear-free boundary conditions, i.e., $\mathbf{n}\cdot\nabla u_\varphi = 0$ at the gas-liquid interface, where $\mathbf{n}$ is the normal vector of the interface within the r-z plane. The volume flux,

$$Q = \iint_{A_l} u_\varphi\, dA_l, \tag{17}$$

and according to Darcy's law,

$$\frac{Q}{A_l} = -\frac{k}{\eta} \frac{\partial P}{R_0 \partial \varphi}, \tag{18}$$

where k is the permeability of the planar meniscus with the unit of m^2. It is determined by the characteristic length of the meniscus, naturally taking r_w. Thus k shall be in the form of

$$k = r_\mathrm{w}^2 \bar{k}(\theta). \tag{19}$$

Here, $\bar{k}(\theta)$, as a function of wettability, describes the effect of the meniscus shape and is obtained numerically, see Appendix A for details. The dissipation function is then expressed as

$$\Phi = \frac{1}{2} \int_0^{\varphi_\mathrm{m}} Q \frac{\partial P}{\partial \varphi}\, d\varphi = \frac{1}{2} \int_0^{\varphi_\mathrm{m}} \frac{Q^2}{A_l} \frac{\eta R_0}{k}\, d\varphi. \tag{20}$$

Considering $\dot{F}$ and Φ are expressed with respect to Q, the Rayleighian is given as

$$\mathscr{R} = \dot{F} + \Phi = \int_0^{\varphi_\mathrm{m}} \frac{\partial a'/A'_l}{\partial \varphi} Q + \frac{1}{2} \frac{Q^2}{A_l} \frac{\eta R_0}{k}\, d\varphi. \tag{21}$$

The governing equation is derived from the Onsager variational principle, $\delta\mathscr{R}/\delta Q = 0$,

$$Q = -\frac{2A_l k}{\eta R_0} \frac{\partial a'/A'_l}{\partial \varphi}. \tag{22}$$

Using the conservation equation Eq. 13 again, we express the governing equation concerning r_w,

$$\dot{r}_\mathrm{w} = \frac{1}{A'_l} \frac{\partial}{\partial \varphi} \left(\frac{2A_l k}{\eta R_0} \frac{\partial a'/A'_l}{\partial \varphi} \right). \tag{23}$$

Substituting h, A_l and k in Eq. 23, a dimensionless form of the governing equation is obtained,

$$r_\mathrm{w} \dot{r}_\mathrm{w} = \frac{\partial}{\partial \varphi} \left(r_\mathrm{w}^2 \frac{\partial r_\mathrm{w}}{\partial \varphi} \right). \tag{24}$$

Its length is scaled by R_0 and time is scaled by a characteristic time t^*

$$t^* = \frac{2\eta R_0}{\gamma(\cos\theta - \sin\theta)\bar{k}}. \tag{25}$$

2.2 Theoretical analysis

The time evolution equation Eq. 24 suggests a scaling relationship,

$$r_\mathrm{w} \sim \frac{\varphi^2}{t}, \tag{26}$$

and thus it admits a self-similar solution in the form of

$$r_\mathrm{w}(\varphi, t) = H(\chi),\, \chi = \frac{\varphi^2}{t}, \tag{27}$$

where $H(\cdot)$ is a function to be determined. Substituting Eq. 27 into Eq. 24, it gives an ordinary differential equation,

$$2HH' + (8H'^2 + 4H''H + H')\chi = 0, \tag{28}$$

where the prime represents the derivative regarding χ. When $\chi = 0$, it corresponds to the boundary condition at the liquid source ($\varphi = 0$), i.e., $H(0) = r_\mathrm{w}|_{\varphi=0} > 0$, and from Eq. 28 it leads to

$$H'(0) = 0. \tag{29}$$

Another boundary condition is at the liquid front where $H(\chi)$ approaches zero at a certain value $\chi = \chi_0$, i.e.,

$$H(\chi_0) = 0. \tag{30}$$

Substituting Eq. 30 in Eq. 28, we obtain

$$H'(\chi_0) = -\frac{1}{8}. \tag{31}$$

To satisfy Eq. 30 and 31, $H(\chi)$ is assumed to be in form of

$$H(\chi) = \Sigma_i a_i(\chi_0 - \chi)^{n_i} + \frac{1}{8}(\chi_0 - \chi), \tag{32}$$

where parameters n_i and a_i are to be determined. According to Eq. 29, we obtain

$$\Sigma_i a_i n_i \chi_0^{n_i} = -\frac{1}{8}\chi_0. \tag{33}$$

We consider a situation with a fixed r_w at the liquid source ($\varphi = 0$) i.e., $r_\mathrm{w}|_{\varphi=0} = r_\mathrm{w}^0$, and it leads to

$$H(0) = \Sigma_i a_i \chi_0^{n_i} + \frac{1}{8}\chi_0 = r_\mathrm{w}^0. \tag{34}$$

Anticipating $n_i > 1$, the upper and lower bounds of $\Sigma_i a_i \chi_0^{n_i}$ are determined from Eq. 33,

$$-\frac{1}{8n_i^{\min}} = \Sigma_i a_i \frac{n_i}{n_i^{\min}}\chi_0^{n_i} \le \Sigma_i a_i \chi_0^{n_i} \le \Sigma_i a_i \frac{n_i}{n_i^{\max}}\chi_0^{n_i} = -\frac{1}{8n_i^{\max}}, \tag{35}$$

where $n_i^{\max}$ and $n_i^{\min}$ are the maximum and minimum value of n_i. Thus, $\Sigma_i a_i \chi_0^{n_i}$ can be estimated as

$$\Sigma_i a_i \chi_0^{n_i} = -\frac{1}{8\bar{n}}, \tag{36}$$

where $n_i^{\max} \le \bar{n} \le n_i^{\max}$. Furthermore, substituting it into Eq. 34, an asymptotic solution of the liquid front φ_m is obtained,

$$\varphi_\mathrm{m} = \sqrt{\frac{8\bar{n}}{\bar{n} - 1} r_\mathrm{w}^0 t}. \tag{37}$$

It suggests $\varphi_\mathrm{m} \sim t^{1/2}$ which aligns with the liquid imbibition in a capillary tube or a homogeneous porous media described by the Lucas-Washburn equation (Cai et al., 2022). Furthermore, the merging time t_merge, at which two liquid fronts from both sides touch each other can be estimated. Here, we only consider the contribution of the linear term in Eq. 32, and by letting $\varphi_\mathrm{m} = \pi$,

$$t_\mathrm{merge} \approx \frac{\pi^2}{8 r_\mathrm{w}^0}. \tag{38}$$

2.3 Numerical solution

We now numerically solve the time-evolution equation Eq. 24 for validating our proposed law $\varphi_\mathrm{m} \sim t^{1/2}$. Besides the boundary condition at the liquid source ($\varphi = 0$), the one at the merging point ($\varphi = \pi$) is set as $r_\mathrm{w}|_{\varphi=\pi} = r_\mathrm{w}^\mathrm{min}$. Then, the capillary pressure is calculated as per Eq. 15,

$$P_\mathrm{c} = \gamma \left(\frac{1}{r_\mathrm{w}^0} - \frac{1}{r_\mathrm{w}^\mathrm{min}} \right) \frac{\cos\theta - \sin\theta}{\bar{k}}. \tag{39}$$

Since the liquid front is regarded as a point, $r_\mathrm{w}^\mathrm{min}$ should be zero. However, the capillary pressure would be an infinite value if $r_\mathrm{w}^\mathrm{min} = 0$ as per Eq. 39, resulting in a convergence issue. Therefore, we take a finitely small value as $r_\mathrm{w}^\mathrm{min}$, and r_w is initialized with $r_\mathrm{w}^\mathrm{min}$, i.e., $r_\mathrm{w}|_{t=0} = r_\mathrm{w}^\mathrm{min}$. The Eq. 24 with the boundary conditions is solved on a domain $\varphi \in [0, \pi]$ using the finite element method.

We first investigate the effect of $r_\mathrm{w}^\mathrm{min}$. As shown in figure 2, cases with $r_\mathrm{w}^\mathrm{min}$ ranging from 3e−5 to 1e−3 are almost overlapped regarding the time evolution of the liquid front position in figure 2(a) and the r_w profiles in figure 2(b). A difference is observed in the zoom-in plot around the liquid front in figure 2(b), suggesting that the value of $r_\mathrm{w}^\mathrm{min}$ only influences the local region in the vicinity of the liquid front. More importantly, the measured log-log slope of curves φ_m vs. t, as shown in figure 2(a), confirms $\varphi_\mathrm{m} \sim t^{1/2}$ at late times.

Another scaling law that $\varphi_\mathrm{m} \sim \sqrt{r_\mathrm{w}^0}$, suggested by Eq. 37, is rationalized and verified. From Eq.39, it suggests that the larger r_w^0 is, the stronger P_c is and thus the faster the wetting film spreads along the corner. Furthermore, as shown in figure 3(a), cases with various r_w^0 ranging from 0.03 to 0.12 collapsed as one line on the $\varphi_\mathrm{m}/\sqrt{r_\mathrm{w}^0}$-$t$ space. In addition, the merging time t_merge for each case is directly measured from the numerical result and compared against the theoretical estimation from Eq. 38. Figure 3(b) shows that both numerical solutions and theoretical estimations have the same trend, but Eq. 38 underestimates t_merge as per the comparison. This inconsistency should be attributed to the transition period at the early time, as can be seen in figure 3(a). During the transition period, the interfacial profile is relaxed and self-adjusted to progressively follow the law $\varphi_\mathrm{m} \sim t^{1/2}$. Nevertheless, predicting the transition period is out of the scope of the theoretical model.

3 Volume-of-Fluid simulation

Given that our theoretical model is developed on the foundational assumption of the ”arc-shape interface”, it is necessary to gauge the practical applicability of our theoretical model and further test the proposed scaling law. In this section, we will conduct numerical simulations using the Volume-of-Fluid (VoF) method. Not only for the verification, we also investigate the film wrapping problems under diverse conditions.

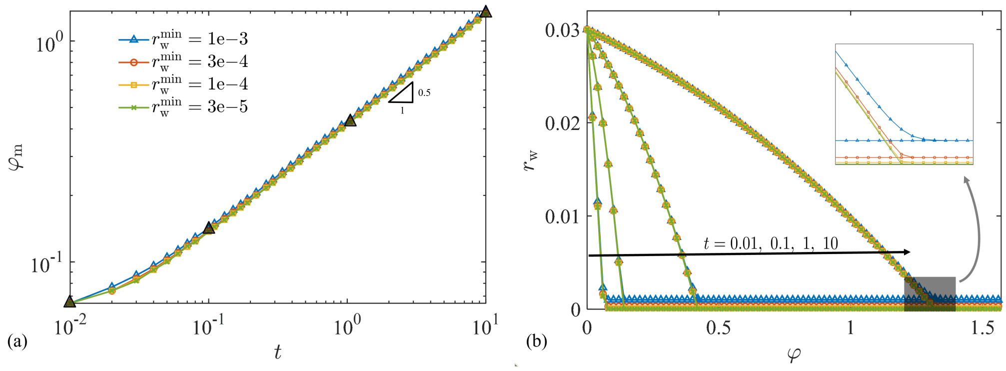

Figure 2. (a) The evolution of φ_m of cases with $r_w^0 = 0.03$ and various $r_w^{min} \in [1e-3, 3e-4, 1e-4, 3e-5]$. (b) The corresponding r_w profiles at different times which are marked by black triangles in (a), and the insert is a zoom-in plot of liquid fronts.

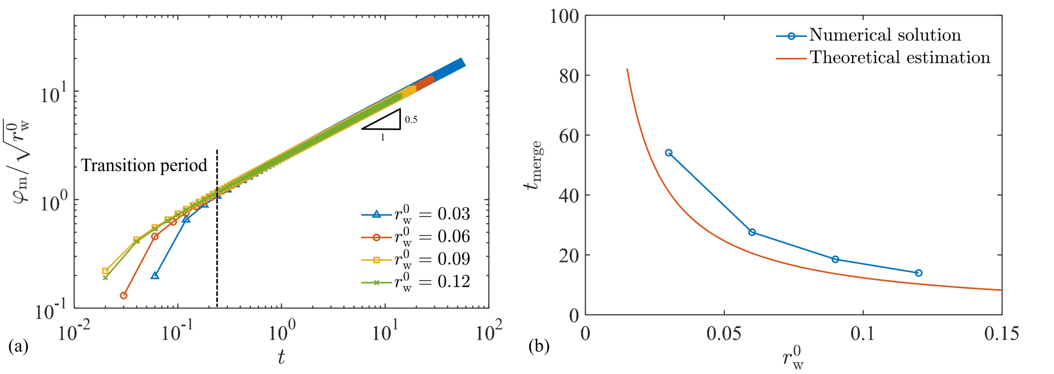

Figure 3. (a) The evolution of scaled φ_m of cases with $r_w^{min} = 3e-4$ and various $r_w^0 \in [0.03, 0.06, 0.09, 0.12]$. (b) The comparison of t_{merge} obtained from the numerical solution and theoretical estimation (Eq. 38) under various r_w^0.

3.1 Governing equations

We consider the imbibition as a laminar, incompressible, and immiscible two-phase flow, which is governed by the Navier-Stokes equations,

$$\begin{aligned} \nabla \cdot \boldsymbol{v} &= 0, && (40)\\ \rho \partial \boldsymbol{v}/\partial t + \rho \nabla \cdot (\boldsymbol{v}\boldsymbol{v}) &= -\nabla p + \mu \nabla^2 \boldsymbol{v} + \boldsymbol{F}_\gamma, && (41) \end{aligned}$$

where $\boldsymbol{v}$ denotes the velocity vector; p, ρ, μ are respectively the fluid pressure, density and viscosity; $\boldsymbol{F}_\gamma$ is the surface tension force per unit volume. The interface between two phases is tracked by the volume-of-fluid (Vof) method, wherein a scalar transport equation regarding volume fraction α is introduced,

$$\partial \alpha/\partial t + \nabla \cdot (\boldsymbol{v}\alpha) = 0. \tag{42}$$

The interface is reconstructed based on α-field and related geometric features including interface normal $\boldsymbol{n}_\alpha$ and curvature κ are obtained. Then, $\boldsymbol{F}_\gamma$ is calculated as (Brackbill et al., 1992)

$$\boldsymbol{F}_\gamma = \gamma \kappa \nabla \alpha, \tag{43}$$

Wetting conditions are implemented by correcting the $\boldsymbol{n}_\alpha$ in the vicinity of the solid walls (Saha & Mitra, 2009),

$$\boldsymbol{n}_\alpha = \boldsymbol{n}_s \cos\theta + \boldsymbol{t}_s \sin\theta, \tag{44}$$

where $\boldsymbol{n}_s$ and $\boldsymbol{t}_s$ are the unit normal and tangent vectors to solid walls, respectively. Eq. 40-42 with the following boundary conditions are solved using OpenFOAM (Roenby et al., 2016; Scheufler & Roenby, 2019).

3.2 Numerical model

We build up a three-dimensional numerical model, as shown in figure 4(a). Considering this problem is a symmetric one, a half-cylinder zone is adopted as the computation domain. The symmetry plane, as marked by dash-dot lines in figure 4(b), is divided by the cylinder wall into two face boundaries, i.e., the left and right face. At the right face, where the liquid fronts from both sides will touch, symmetric boundary conditions are imposed for the flow field and the α field. At the left face, we control the α field to simulate different types of the liquid source, including the "fixed boundary" mimicking the situation where r_w is fixed at the liquid source and the "free boundary" where r_w can freely grow at the liquid source as described in detail in the following. Wetting wall boundary conditions are set on the cylinder wall and the bottom wall, as marked in figure 4(a), following Eq. 44. Other boundaries connect to the environment and thus a zero-pressure condition and a zero-gradient α field are imposed.

The radius of the domain is $3R_0$ and its height is $2R_0$. The upper limit of mesh size is set as $R_0/100$, which has passed the mesh-sensitive test. We set the viscosity ratio as 100 which is large enough to represent a gas-liquid situation. The quantities including r_w, h_w, φ_m are directly measured from the reconstructed interface. For the convenience of comparing with the theoretical model, all lengths and times presented in the following have been scaled by R_0 and t^* separately.

3.2.1 Fixed boundary

We firstly simulate the situation with fixed α field at the left face, which is expected to agree with the theoretical predictions in Section 2.2. Specifically, provided r_w^0 and θ, the interface position at the left face is calculated as per Eq. 1, and then the liquid and gas phase separated by the interface are mapped on the α field at the left face.

We conduct simulations over a range of $r_\mathrm{w}^0 \in [0.3, 0.5]$ and $\theta \in [15°, 20°, 25°, 30°]$. Figure 5(a) shows the evolution of φ_m scaled by $\sqrt{r_\mathrm{w}^0}$ in the log-log space. For the group

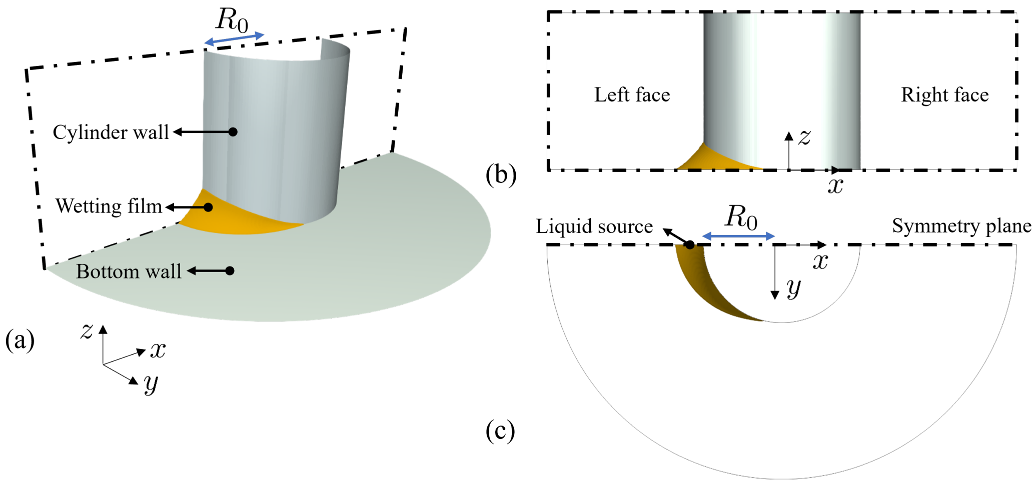

Figure 4. Geometrical settings of the numerical model in a perspective (a), front (b), and top view (c).

of cases with the same r_w^0, simulation results from various-θ cases are overlapped, suggesting that the effect of wettability is well considered in t^*. Moreover, the scaling law $\varphi_\mathrm{m} \sim \sqrt{r_\mathrm{w}^0}$ is also verified to a good extent, since the two groups are significantly close to each other and almost collapse as one line, though a small gap is observed. To better provide insights into the evolution of φ_m, we calculate the secant slopes of φ_m-t curves in the log-log space, as defined as

$$\frac{\Delta \log \varphi_\mathrm{m}}{\Delta \log t} = \frac{\log \frac{\varphi_\mathrm{m}(t+\mathrm{d}t)}{\varphi_\mathrm{m}(t-\mathrm{d}t)}}{\log \frac{t+\mathrm{d}t}{t-\mathrm{d}t}}, \tag{45}$$

where dt is the scaled time interval. As shown in figure 5(b), each case has a transition period at the early time, during which the secant slope sharply decreases from a large value and then becomes flattened. The length of such a transition period depends on r_w^0 and θ, but it generally takes around $2t^*$ before the evolution reaches the steady state. The steady slope, though floating over a range of $[0.47, 0.55]$, is close to 0.5, indicating that the proposed law $\varphi_\mathrm{m} \sim t^{1/2}$ effectively governs the imbibition dynamics. Besides, t_merge measured from simulation results is compared with the theoretical estimation from Eq. 38, as presented in figure 5(c). The scaled t_merge seems a function of θ, while it should be independent of θ according to the theoretical model where the impacts of θ have been considered in t^*. This is owing to the transition period which is θ-dependent and involved in the measured t_merge. Although deviations between predicted and measured t_merge are observed, the theoretical model provides a reasonable lower-bound estimation of t_merge.

What's more, to further confirm the practicability of our theoretical model, we test the foundational assumption that the interface on the r-z plane maintains arc-shape. Figure 5(d) shows the evolution of h_w-r_w at $\varphi = \pi/2$ of each case. With imbibition ongoing, the wetting film expands within the r-z plane and h_w should increase at the same rate with r_w as per the assumption, i.e., $r_\mathrm{w} = h_\mathrm{w}$ as marked by the dashed line in figure 5(d). It is observed that the measured r_w-h_w aligns well with the assumption, especially at the early time when r_w is small. With r_w increasing, though a slight deviation occurs, i.e., h_w becomes smaller than r_w, the assumption is still acceptable. Noteworthily, this deviation is only determined by the relative size of the wetting film to the cylinder radius. In our theoretical model, only the curvature within the r-z plane is considered for calculating the capillary pressure. However, with the wetting film expanding and r_w increasing to close to 1, the contribution of the other principle curvature to

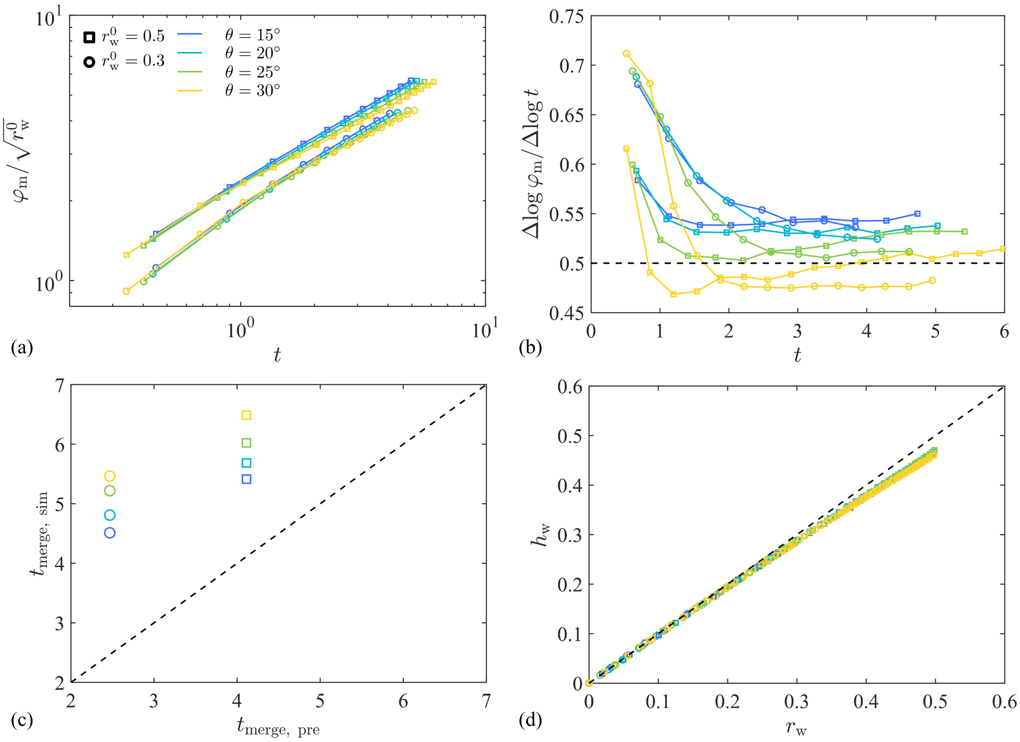

Figure 5. Simulation results of the fixed-boundary situation with $r_w^0 \in [0.3, 0.5]$ and $\theta \in [15°, 20°, 25°, 30°]$. The evolution of (a) the scaled φ_m and (b) the corresponding secant slope. (c) The comparison of t_{merge} against the theoretical prediction. (d) The wetting height h_w vs. the wetting width r_w at $\varphi = \pi/2$.

the capillary pressure may not be neglected. Thus, the effective scope of our theoretical model should be limited to the "small-film-size" regime. Additionally, the deviation from the "arc-shape interface" assumption could be another source of the failure in precisely predicting t_{merge}.

3.2.2 Free boundary

We then extend our focus to another situation where the size of the wetting film at the liquid source can freely grow. Correspondingly, the zero-gradient boundary condition for α field is imposed at the left face.

The simulation cases cover various $\theta \in [15°, 20°, 25°, 30°]$. Initially, a small arc-shape patch (around $0.05R_0$) is set as a liquid phase at the corner of the left face. It relaxes and evolves to form a meniscus after one recording time step dt. We regard the size of such formed meniscus as a initial value r_w^0 at the liquid source, which depends on θ, as shown in figure 6(a). However, since growth curves under various θ are observed paralleled, the growths of r_w at the liquid source are in a similar track, approximately following a power law. The average power is measured as 0.23, which is marked in figure 6(b). Equivalently, as for the theoretical model, the boundary at the liquid source $r_w|_{\varphi=0}$ is time-dependent, i.e.,

$$r_w|_{\varphi=0} \approx r_w^0 t^{0.23}. \tag{46}$$

The analysis in Section 2.2 maintains effective but an adaption is needed. Considering the transient formation of $r_\mathrm{w}|_{\varphi=0}$, Eq. 37 is modified as

$$\varphi_\mathrm{m} \approx \sqrt{\frac{8\bar{n}}{\bar{n}-1} r_\mathrm{w}^0 t^{1.23}}. \tag{47}$$

Thus, we obtain an approximate scaling law $\varphi_\mathrm{m} \sim t^{0.615}$ adapted to the free-boundary situation. The liquid front position is measured from our simulation results, and its evolution and secant slopes are demonstrated in figure 6(c) and (d). Similarly, after a transition period, liquid front advancing reaches a steady state. The steady slope of each case tends to be around 0.6, as marked in figure 6(d), which is comparable to the theoretically predicted value 0.615. Moreover, based on the Eq. 47, we can estimate t_merge as

$$t_\mathrm{merge} \approx \left(\frac{\pi^2}{8 r_\mathrm{w}^0}\right)^{\frac{1}{1.23}}. \tag{48}$$

This estimation still serves as a lower bound of t_merge, as observed in figure 6(e). Again, we test the foundational assumption of the "arc-shape interface" in the free-boundary situation using h_w-r_w on the $\varphi = \pi/2$ plane. As shown in figure 6(f), the deviation is linearly enlarged with r_w, and the relative error $(r_\mathrm{w} - h_\mathrm{w})/r_\mathrm{w}$ is larger than 10% when $r_\mathrm{w} = 0.8$, probably suggesting that the contribution of the secondary principle curvature has to be considered if r_w further increases.

We now shift our focus to imbibition dynamics after merging. Though post-merging behaviours are beyond the scope of the theoretical model, our simulation results provide insights into them. After the two fronts merge at the right face, the film continues to expand in the free-boundary situation. We show the evolution of r_w at the right face in figure 7(a) and the secant slopes in figure 7(b). The expanding rate of r_w decreases at the beginning and gradually tends to be a constant value, i.e., 1.11 as marked in figure 7(b). In another word, r_w increases with time approximately in a linear mode, which is significantly faster compared to the one at the liquid source, see figure 6(b).

4 Conclusion

In this work, We have theoretically and numerically investigated the spontaneous imbibition of a liquid wetting a cylinder corner. Using the Onsager variational principle, a time evolution equation for the meniscus profile was built up. Based on the time evolution equation, we derived an asymptotic solution of the liquid front $\varphi_\mathrm{m} \sim \sqrt{r_\mathrm{w}^0 t}$. It suggests that the advance of the liquid front follows the Lucas-Washburn kinetics, i.e., the $t^{1/2}$ scaling, if the boundary r_w^0 is time-independent; otherwise, the effect of the dynamic boundary should be included and the scaling accordingly changes. Then, the imbibition process was numerically simulated using VoF method, and the simulation results can be well rationalized by our proposed scaling law to a large extent. Furthermore, we provide a theoretical prediction of t_merge, which is demonstrated as a lower bound of the real one.

Our theoretical model is extensible. More complex geometries, such as tapered, ellipse, or even any arbitrary-shape symmetric cylinders, can be modelled by modifying the expression of the free energy. We can expect the scaling coefficient C and characteristic time t^* varies with the geometry while the scaling $t^{1/2}$ maintains effective. Moreover, another demanding aspect for future works is to investigate the imbibtion flows in a cylinder group, and model how the liquid front spreads among neighboring cylinders.

Appendix A Determination of $\bar{k}(\theta)$

We determine the relative permeability $\bar{k}(\theta)$ using numerical experiments. Eq. 16 is solved on a axisymmetric meniscus domain, as shown in figure A1, whose geometry

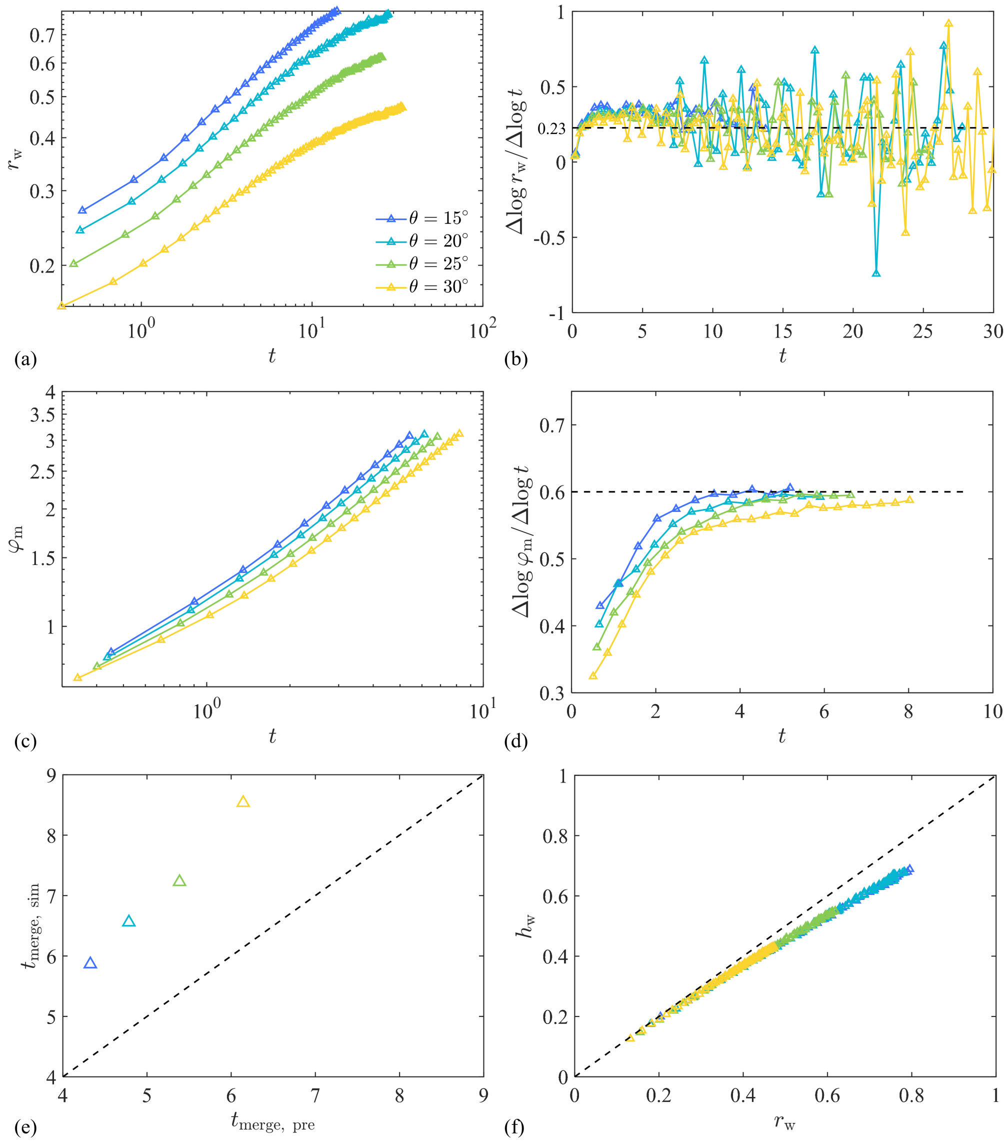

Figure 6. Simulation results of the free-boundary situation with $\theta \in [15^\circ, 20^\circ, 25^\circ, 30^\circ]$. The evolution of (a) r_w at the liquid source and (b) the corresponding secant slope. The evolution of (c) φ_m and (d) the corresponding secant slope. (e) The comparison of t_merge against the theoretical prediction. (f) The wetting height h_w vs. the wetting width r_w at $\varphi = \pi/2$.

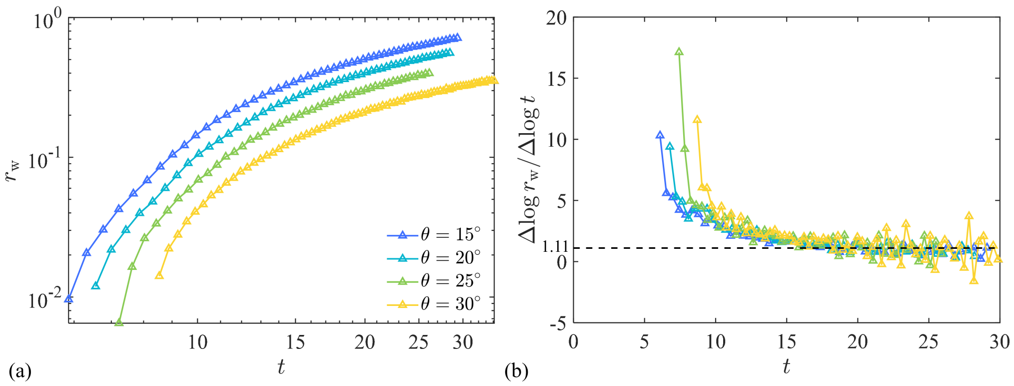

Figure 7. The post-merging dynamics of the free-boundary situation including (a) the evolution of rw at the right face and (b) the corresponding secant slope.

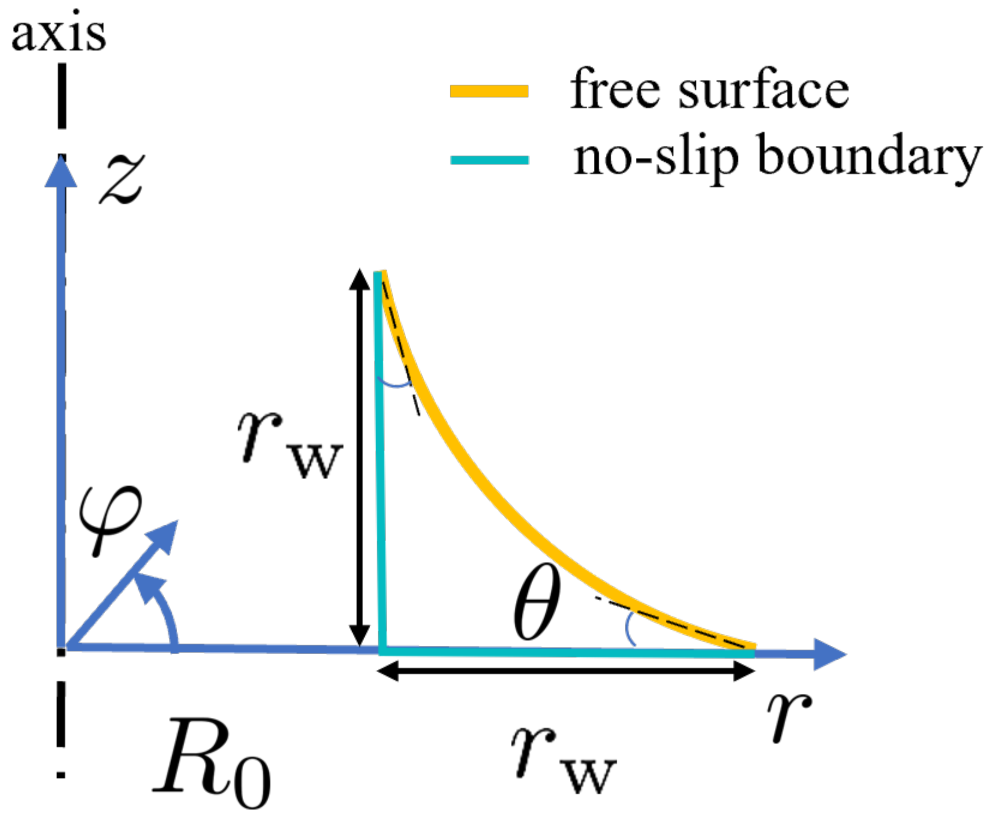

Figure A1. The computation model for determining the relative permeability $\bar{k}(\theta)$

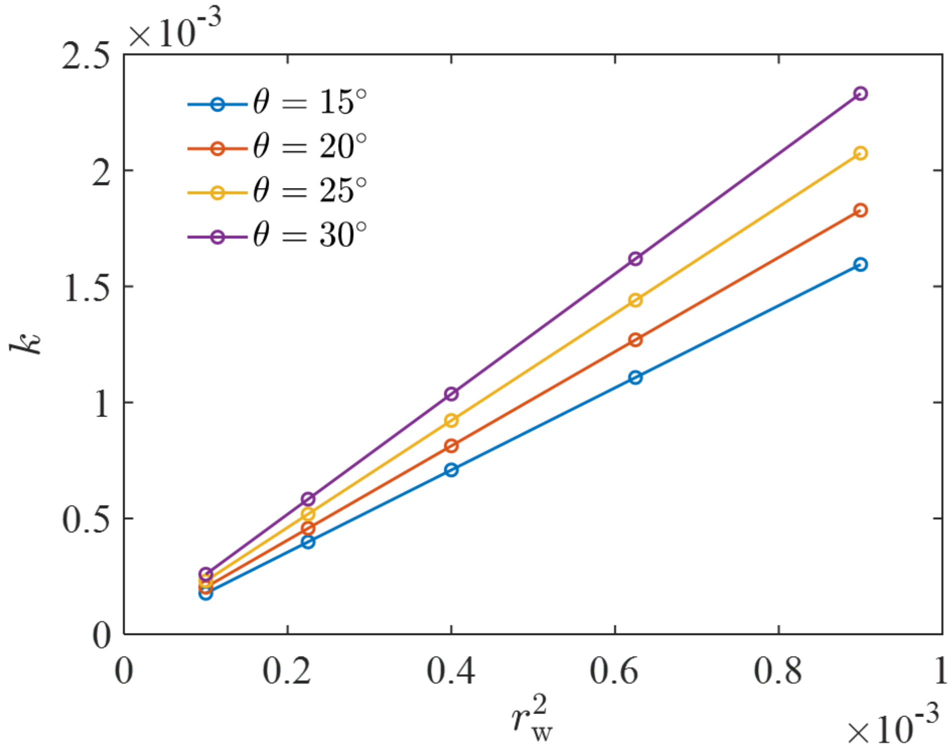

Figure A2. The permeability k vs. r_w^2 for various θ.

Table A1. Relative permeability $\bar{k}(\theta)$

15°	20°	25°	30°
0.01772	0.02032	0.02305	0.02591

is dependent on θ and r_w. We sweep the parameter combinations of $\theta \in [15°, 20°, 25°, 30°]$ and $r_\mathrm{w} \in [0.10, 0.15, 0.20, 0.25, 0.30]$, and calculate the permeability k according to Eq. 18. Figure A2 shows that the permeability k is proportional to r_w^2 for any θ. Thus, the relative permeability $\bar{k}(\theta)$ can be obtained by measuring the slope of k-r_w^2 lines, which are summarized in table A1.

Acknowledgments

References

Brackbill, J. U., Kothe, D. B., & Zemach, C. (1992). A continuum method for modeling surface tension. *Journal of computational physics*, *100*(2), 335–354.

Cai, J., Chen, Y., Liu, Y., Li, S., & Sun, C. (2022). Capillary imbibition and flow of wetting liquid in irregular capillaries: A 100-year review. *Advances in Colloid and Interface Science*, *304*, 102654.

Cai, J., Jin, T., Kou, J., Zou, S., Xiao, J., & Meng, Q. (2021). Lucas–washburn equation-based modeling of capillary-driven flow in porous systems. *Langmuir*, *37*(5), 1623–1636.

Concus, P., & Finn, R. (1969). On the behavior of a capillary surface in a wedge.

Proceedings of the National Academy of Sciences, *63*(2), 292–299.

Cox, S., Davarpanah, A., & Rossen, W. (2023). Interface shapes in microfluidic porous media: conditions allowing steady, simultaneous two-phase flow. *Transport in Porous Media*, *147*(1), 197–216.

Deng, D., Tang, Y., Zeng, J., Yang, S., & Shao, H. (2014). Characterization of capillary rise dynamics in parallel micro v-grooves. *International Journal of Heat and Mass Transfer*, *77*, 311–320.

Doi, M. (2013). *Soft matter physics.* Oxford University Press, USA.

Gurumurthy, V. T., Rettenmaier, D., Roisman, I. V., Tropea, C., & Garoff, S. (2018). Computations of spontaneous rise of a rivulet in a corner of a vertical square capillary. *Colloids and Surfaces A: Physicochemical and Engineering Aspects*, *544*, 118–126.

Ha, J., Kim, J., Jung, Y., Yun, G., Kim, D.-N., & Kim, H.-Y. (2018). Poro-elasto-capillary wicking of cellulose sponges. *Science advances*, *4*(3), eaao7051.

Higuera, F., Medina, A., & Linan, A. (2008). Capillary rise of a liquid between two vertical plates making a small angle. *Physics of Fluids*, *20*(10).

Hu, R., Wan, J., Yang, Z., Chen, Y.-F., & Tokunaga, T. (2018). Wettability and flow rate impacts on immiscible displacement: A theoretical model. *Geophysical Research Letters*, *45*(7), 3077–3086.

Primkulov, B. K., Pahlavan, A. A., Fu, X., Zhao, B., MacMinn, C. W., & Juanes, R. (2021). Wettability and lenormand's diagram. *Journal of Fluid Mechanics*, *923*, A34.

Roenby, J., Bredmose, H., & Jasak, H. (2016). A computational method for sharp interface advection. *Royal Society open science*, *3*(11), 160405.

Rye, R., Yost, F., & Mann, J. (1996). Wetting kinetics in surface capillary grooves. *Langmuir*, *12*(20), 4625–4627.

Saha, A. A., & Mitra, S. K. (2009). Effect of dynamic contact angle in a volume of fluid (vof) model for a microfluidic capillary flow. *Journal of colloid and interface science*, *339*(2), 461–480.

Scheufler, H., & Roenby, J. (2019). Accurate and efficient surface reconstruction from volume fraction data on general meshes. *Journal of computational physics*, *383*, 1–23.

Suo, S., Liu, M., & Gan, Y. (2019). Modelling imbibition processes in heterogeneous porous media. *Transport in Porous Media*, *126*, 615–631.

Tang, L.-H., & Tang, Y. (1994). Capillary rise in tubes with sharp grooves. *Journal de Physique II*, *4*(5), 881–890.

Washburn, E. W. (1921). The dynamics of capillary flow. *Physical review*, *17*(3), 273.

Weislogel, M. M. (2012). Compound capillary rise. *Journal of Fluid Mechanics*, *709*, 622–647.

Yu, T., Zhou, J., & Doi, M. (2018). Capillary imbibition in a square tube. *Soft Matter*, *14*(45), 9263–9270.

Zhao, B., MacMinn, C. W., & Juanes, R. (2016). Wettability control on multiphase flow in patterned microfluidics. *Proceedings of the National Academy of Sciences*, *113*(37), 10251–10256.

Zhao, B., MacMinn, C. W., Primkulov, B. K., Chen, Y., Valocchi, A. J., Zhao, J., ... others (2019). Comprehensive comparison of pore-scale models for multiphase flow in porous media. *Proceedings of the National Academy of Sciences*, *116*(28), 13799–13806.

Zhao, J., Qin, F., Fischer, R., Kang, Q., Derome, D., & Carmeliet, J. (2021). Spontaneous imbibition in a square tube with corner films: theoretical model and numerical simulation. *Water Resources Research*, *57*(2), e2020WR029190.

Zhou, J., & Doi, M. (2020). Universality of capillary rising in corners. *Journal of Fluid Mechanics*, *900*, A29.

Spontaneous imbibition of a wetting film wrapping a cylinder corner

Si Suo[1]

[1]Linné Flow Centre, KTH Royal Institute of Technology, Department of Engineering Mechanics, 10044 Stockholm, Sweden.

Key Points:

- A combined theoretical and numerical approach is employed to investigate the imbibition dynamics of wetting film wrapping a cylinder corner.
- The advance of liquid front generally follows the Lucas-Washburn kinetics but also depends on the boundary dynamics.
- A theoretical estimation of time lengths is provided in which wettability and liquid properties are well considered.

Corresponding author: Si Suo, `ssuo@kth.se`

Abstract

Spontaneous imbibition flows within confined geometries are commonly encountered in both natural phenomena and industrial applications. A profound knowledge of the underlying flow dynamics benefits a broad spectrum of engineering practices. Nonetheless, within this area, especially concerning complex geometries, there exists a substantial research gap. This work centers on the cylinder-plane geometry, employing a combined theoretical and numerical approach to investigate the process of a wetting film wrapping a cylinder corner. It is found that the advance of the liquid front generally follows the Lucas-Washburn kinetics, i.e., $t^{1/2}$ scaling, but it also depends on the dynamics of the liquid source. Furthermore, we provide a theoretical estimation of the timescale associated with the imbibition process. Notably, this timescale is highly dependent on the wettability condition and the properties of the involved liquid. Importantly, the practicability of our theoretical framework is well confirmed by the numerical experiments.

1 Introduction

Spontaneous imbibition flows, i.e, liquids driven by capillary pressure to wet confined geometries, such as capillary tubes (Cai et al., 2021), grooves (Tang & Tang, 1994; Deng et al., 2014), porous media (Suo et al., 2019; Ha et al., 2018), etc., serves a crucial role in various natural and industrial processes. The pioneering research dates back to the Lucas-Washburn equation (Washburn, 1921), which leads to a scaling law regarding the evolution of the liquid front $h(t)$ in capillaries, i.e., $h = Ct^{1/2}$. This type of scaling law describes a energy balance between the capillary and viscous terms. Specifically, the wetting liquid is driven by the capillary force to spread on the surface and tends to maximize the coverage over the surface, during which the interfacial energy decreases and is consumed by the viscous friction. When the gravity is considered, part of releasing interfacial energy is transformed to the gravity potential leading to a different $t^{1/3}$ scaling. Nevertheless, the Lucas-Washburn equation was developed for circular capillaries. Once the confined geometry is complex, to what extent the $t^{1/2}$ scaling can predict the imbibition dynamics and how to estimate the scaling coefficient C remains unexplored, especially when sharp corners come up in a geometry.

There have been certain works appealing to imbibition in corners. For a open V-shape groove, Tang and Tang (1994) theoretically proved that the imbibition dynamics follow the scaling $t^{1/2}$ ignoring the gravity or $t^{1/3}$ considering the gravity; Higuera et al. (2008) derived the same scaling law within the framework of the lubrication approximation. These scaling laws have been verified against the experimental observations (Higuera et al., 2008; Rye et al., 1996; Deng et al., 2014). Very recently, Zhou and Doi (2020) developed a theory model for corners with curved walls using the Onsager principle. Surprisingly, they found the above scaling law still works while the scaling coefficient C slightly depends on the wall shape. In a closed medium, like a square or rectangular tube, if the contact angle $\theta < 45°$, i.e., the Concus-Finn condition is satisfied (Concus & Finn, 1969), the liquid can wet the interior corners and forms "finger-like" films along the corners. The imbibition flows thus become manifold, i.e., the bulk flow and corner flows, and the synergistic effect of the corner and bulk flow should be carefully considered (Weislogel, 2012). Imbibition in square tubes have been numerically and theoretically investigated (Yu et al., 2018; J. Zhao et al., 2021; Gurumurthy et al., 2018). It is found that both flows follow the Lucas-Washburn kinetics and their coupling plays an evident role.

What's more complex, in a porous medium, especially a natural one, the inter-connected angular channels randomly distribute in its solid space, where corner flows are enhanced and bulk-corner flows are expected to interplay in a more complicated manner. Cylinder-based geometries are commonly used as a surrogate model of real porous media. A quantity of experimental and numerical works have been reported based on this geometrical

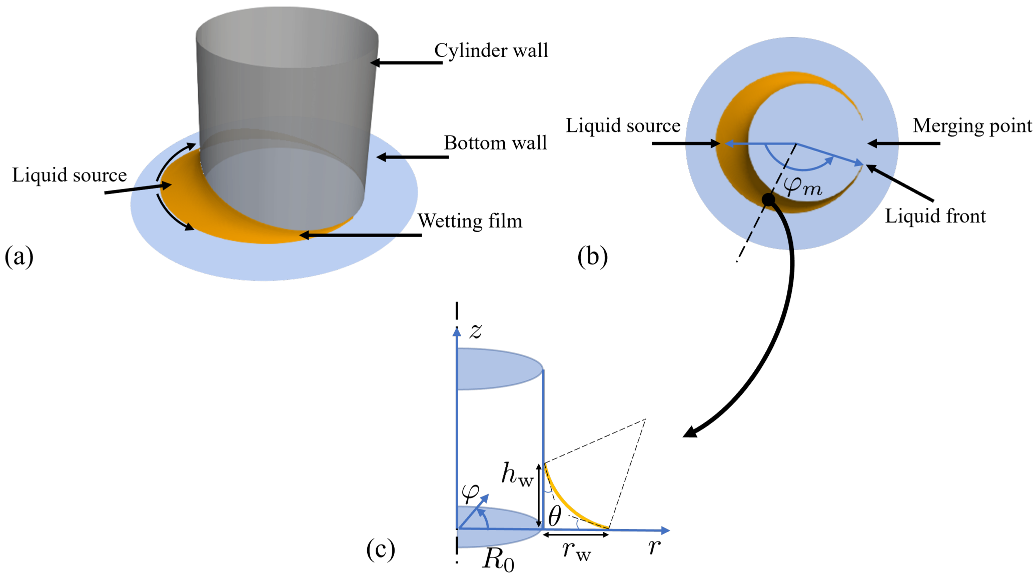

Figure 1. Schematics of the theoretical model, including a perspective view (a), a top view (b) and a sectional profile on the r-z plane of a cylindrical coordinate (c).

settings. B. Zhao et al. (2016) conducted a microfluidic experiment and directly visualized the process of liquid film spreading among cylinder corners in the strong imbibition regime ($\theta < 30°$). Numerical modelling works on corner flows in cylinder-based porous media are ensued (Primkulov et al., 2021; B. Zhao et al., 2019; Cox et al., 2023; Hu et al., 2018), and the corner flow is regarded as a specific flui-fluid diplacement pattern and emerges under certain combining conditions of capillary number, viscosity ratio and wettability.

Though a great progress regarding spontaneous imbibition flows within complex geometries has been made, answers to the fundamental questions posted in the beginning are still demanding because they are step stones towards better engineering practices. In this work, we shall focus on the cylinder-plane geometry and investigate the process of a liquid film wrapping a cylinder theoretically and numerically.

2 Theoretical model

We consider a film-cylinder system, as shown in figure 1(a). In this setting, a wetting film symmetrically spreads along the cylinder-bottom corner from a liquid source and finally merges at the other end. For describing this problem, a cylindrical coordinate (r-φ-z) is set up, where the liquid source locates at $\varphi = 0$ while the liquid front at $\varphi = \varphi_{\mathrm{m}}$, as can be seen in figure 1(b). Here, we assume that the characteristic size of the liquid film is smaller than the capillary length $l_c = \sqrt{\gamma/\rho g}$, where ρg is the liquid gravity and γ is the surface tension, so that the effect of gravity can be neglected. Additionally, we assume that the liquid-gas interface on the z-r plane is an arc, as shown in figure 1(c). Thus, the wetting height h_{w} and width r_{w} are equal. Provided the wettability condition θ and wetting width r_{w}, the film thickness h as a function of r is expressed as

$$h = R\cos\theta - \sqrt{R^2 - (r - R\cos\theta - R_0)}, \tag{1}$$

where R_0 is the cylinder radius and $R = r_{\mathrm{w}}/(\cos\theta - \sin\theta)$.

78 ### 2.1 Time evolution equation

Using the Onsager principle, we derive the time evolution equation for the meniscus profile, which can be characterized by $r_{\mathrm{w}}(\varphi, t)$ for a given θ as per Eq. 1. For the present problem, it is stated in this principle that the dynamics of the system can be directly determined by the minimum of the Rayleighian (Doi, 2013),

$$\mathscr{R}\left[\dot{r}_{\mathrm{w}}(\varphi, t)\right]=\dot{F}\left[\dot{r}_{\mathrm{w}}(\varphi, t)\right]+\Phi\left[\dot{r}_{\mathrm{w}}(\varphi, t)\right], \tag{2}$$

79 where $\dot{F}$ is the change rate of the free energy of the film-cylinder system; and Φ is the
80 energy dissipation function.

81 #### *2.1.1 The change rate of free energy*

The free energy of the system is a superposition of the interfacial energies along the liquid-cylinder wetting area $A_{ls1}(r_{\mathrm{w}})$, the liquid-wall wetting area $A_{ls2}(r_{\mathrm{w}})$ and the liquid-gas area $A_{lg}(r_{\mathrm{w}})$, and is given by

$$F=\gamma\left(-A_{ls1}\cos\theta-A_{ls2}\cos\theta+A_{lg}\right), \tag{3}$$

82 where

$$\begin{aligned} A_{ls1}(r_{\mathrm{w}}) &= \int_0^{\varphi_{\mathrm{m}}} h_{\mathrm{w}} R_0\, d\varphi, && (4)\\ A_{ls2}(r_{\mathrm{w}}) &= \int_0^{\varphi_{\mathrm{m}}}\int_{R_0}^{R_0+r_{\mathrm{w}}} r\, dr\, d\varphi, && (5)\\ A_{lg}(r_{\mathrm{w}}) &= \int_0^{\varphi_{\mathrm{m}}}\int_{R_0}^{R_0+r_{\mathrm{w}}} \sqrt{h_r^2+h_\varphi^2/r^2+1}\, r\, dr\, d\varphi, && (6)\end{aligned}$$

and h_r and h_φ are the derivatives of h concerning r and φ, respectively. The change rate of the free energy $\dot{F}$ is thus obtained as

$$\dot{F}=\gamma\dot{r}_{\mathrm{w}}\left(-A_{ls1}'\cos\theta-A_{ls2}'\cos\theta+A_{lg}'\right). \tag{7}$$

83 Here the top dot denotes the time derivative and the prime denotes the derivative with
84 respect to r_{w}. Separately, A_{ls1}' and A_{ls2}' can be directly derived as

$$\begin{aligned} A_{ls1}' &= \int_0^{\varphi_{\mathrm{m}}} R_0\, d\varphi, && (8)\\ A_{ls2}' &= \int_0^{\varphi_{\mathrm{m}}} R_0+r_{\mathrm{w}}\, d\varphi. && (9)\\ & && (10)\end{aligned}$$

As for A_{lg}', since the size film is much thinner than the cylinder radius, i.e., $h \ll R_0$, and moreover $h_\varphi^2/r^2 \ll h_r^2 \ll 1$, A_{lg}' can be given as a simplified form

$$A_{lg}'=\int_0^{\varphi_{\mathrm{m}}}\left[(R_0+r_{\mathrm{w}})+\int_{R_0}^{R_0+r_{\mathrm{w}}} r h_r h_r'\, dr\right] d\varphi. \tag{11}$$

An auxiliary variable $a'(r_{\mathrm{w}})$ is defined as an integrated parts of F for the convenience of following usages, i.e.,

$$a'(r_{\mathrm{w}})=-(2R_0+r_{\mathrm{w}})\cos\theta+(R_0+r_{\mathrm{w}})+\int_{R_0}^{R_0+r_{\mathrm{w}}} r h_r h_r'\, dr. \tag{12}$$

We take the volume flux $Q(\varphi, t)$ of liquid flowing across the cross-section area, showing in figure 1 at φ, as an independent variable. Here, $Q(\varphi, t)$ is related to $\dot{r}_{\mathrm{w}}(\varphi, t)$ by the conservation equation, which reads

$$\frac{\partial A_l}{\partial t}=A_l'\dot{r}_{\mathrm{w}}=-\frac{1}{R_0}\frac{\partial Q}{\partial \varphi}, \tag{13}$$

where $A_l = \int_{R_0}^{R_0+r_\mathrm{w}} h\, dr$ is the cross-sectional area. Using the conservation equation Eq. 13, we can rewrite the change rate of free energy as a function of Q instead of $\dot{r}_\mathrm{w}$,

$$\dot{F} = \frac{\gamma}{R_0} \int_0^{\varphi_\mathrm{m}} \frac{\partial a'/A_l'}{\partial \varphi} Q\, d\varphi. \tag{14}$$

The definition of $\dot{F}$ as Eq. 14 suggests that $\dot{F}$ is a measurement of the power of capillary force. Thus, the capillary pressure P_c of the film-cylinder system can be estimated as

$$P_\mathrm{c} = \frac{\gamma}{R_0} \int_0^{\varphi_\mathrm{m}} \frac{\partial a'/A_l'}{\partial \varphi}\, d\varphi. \tag{15}$$

85 #### *2.1.2 Dissipation function*

Assuming that the liquid imbibes slowly along a cylinder corner, the inertia effect can be neglected. The flow is almost one-dimensional since u_φ is much larger than the u_r and u_z. Thus, flow dynamics can be described by the following Stokes equation

$$\eta \nabla^2 u_\varphi = \frac{\partial P}{R_0 \partial \varphi}, \tag{16}$$

where $\partial P/(R_0\partial\varphi)$ is the pressure gradient along the φ-axis. Provided $\partial P/(R_0\partial\varphi)$, Eq.16 is solved on the domain shown in figure 1 with no-slip boundary conditions, i.e., $u_\varphi = 0$ at the solid walls and shear-free boundary conditions, i.e., $\mathbf{n} \cdot \nabla u_\varphi = 0$ at the gas-liquid interface, where $\mathbf{n}$ is the normal vector of the interface within the r-z plane. The volume flux,

$$Q = \iint_{A_l} u_\varphi\, dA_l, \tag{17}$$

and according to Darcy's law,

$$\frac{Q}{A_l} = -\frac{k}{\eta} \frac{\partial P}{R_0 \partial \varphi}, \tag{18}$$

where k is the permeability of the planar meniscus with the unit of m^2. It is determined by the characteristic length of the meniscus, naturally taking r_w. Thus k shall be in the form of

$$k = r_\mathrm{w}^2 \bar{k}(\theta). \tag{19}$$

Here, $\bar{k}(\theta)$, as a function of wettability, describes the effect of the meniscus shape and is obtained numerically, see Appendix A for details. The dissipation function is then expressed as

$$\Phi = \frac{1}{2} \int_0^{\varphi_\mathrm{m}} Q \frac{\partial P}{\partial \varphi}\, d\varphi = \frac{1}{2} \int_0^{\varphi_\mathrm{m}} \frac{Q^2}{A_l} \frac{\eta R_0}{k}\, d\varphi. \tag{20}$$

Considering $\dot{F}$ and Φ are expressed with respect to Q, the Rayleighian is given as

$$\mathscr{R} = \dot{F} + \Phi = \int_0^{\varphi_\mathrm{m}} \frac{\partial a'/A_l'}{\partial \varphi} Q + \frac{1}{2} \frac{Q^2}{A_l} \frac{\eta R_0}{k}\, d\varphi. \tag{21}$$

The governing equation is derived from the Onsager variational principle, $\delta\mathscr{R}/\delta Q = 0$,

$$Q = -\frac{2 A_l k}{\eta R_0} \frac{\partial a'/A_l'}{\partial \varphi}. \tag{22}$$

Using the conservation equation Eq. 13 again, we express the governing equation concerning r_w,

$$\dot{r}_\mathrm{w} = \frac{1}{A_l'} \frac{\partial}{\partial \varphi} \left(\frac{2 A_l k}{\eta R_0} \frac{\partial a'/A_l'}{\partial \varphi} \right). \tag{23}$$

Substituting h, A_l and k in Eq. 23, a dimensionless form of the governing equation is obtained,

$$r_\mathrm{w} \dot{r}_\mathrm{w} = \frac{\partial}{\partial \varphi} \left(r_\mathrm{w}^2 \frac{\partial r_\mathrm{w}}{\partial \varphi} \right). \tag{24}$$

Its length is scaled by R_0 and time is scaled by a characteristic time t^*

$$t^* = \frac{2\eta R_0}{\gamma(\cos\theta - \sin\theta)\bar{k}}. \tag{25}$$

2.2 Theoretical analysis

The time evolution equation Eq. 24 suggests a scaling relationship,

$$r_{\mathrm{w}} \sim \frac{\varphi^2}{t}, \tag{26}$$

and thus it admits a self-similar solution in the form of

$$r_{\mathrm{w}}(\varphi, t) = H(\chi),\, \chi = \frac{\varphi^2}{t}, \tag{27}$$

where $H(\cdot)$ is a function to be determined. Substituting Eq. 27 into Eq. 24, it gives an ordinary differential equation,

$$2HH' + (8H'^2 + 4H''H + H')\chi = 0, \tag{28}$$

where the prime represents the derivative regarding χ. When $\chi = 0$, it corresponds to the boundary condition at the liquid source ($\varphi = 0$), i.e., $H(0) = r_{\mathrm{w}}|_{\varphi=0} > 0$, and from Eq. 28 it leads to

$$H'(0) = 0. \tag{29}$$

Another boundary condition is at the liquid front where $H(\chi)$ approaches zero at a certain value $\chi = \chi_0$, i.e.,

$$H(\chi_0) = 0. \tag{30}$$

Substituting Eq. 30 in Eq. 28, we obtain

$$H'(\chi_0) = -\frac{1}{8}. \tag{31}$$

To satisfy Eq. 30 and 31, $H(\chi)$ is assumed to be in form of

$$H(\chi) = \Sigma_i a_i (\chi_0 - \chi)^{n_i} + \frac{1}{8}(\chi_0 - \chi), \tag{32}$$

where parameters n_i and a_i are to be determined. According to Eq. 29, we obtain

$$\Sigma_i a_i n_i \chi_0^{n_i} = -\frac{1}{8}\chi_0. \tag{33}$$

We consider a situation with a fixed r_{w} at the liquid source ($\varphi = 0$) i.e., $r_{\mathrm{w}}|_{\varphi=0} = r_{\mathrm{w}}^0$, and it leads to

$$H(0) = \Sigma_i a_i \chi_0^{n_i} + \frac{1}{8}\chi_0 = r_{\mathrm{w}}^0. \tag{34}$$

Anticipating $n_i > 1$, the upper and lower bounds of $\Sigma_i a_i \chi_0^{n_i}$ are determined from Eq. 33,

$$-\frac{1}{8n_i^{\min}} = \Sigma_i a_i \frac{n_i}{n_i^{\min}} \chi_0^{n_i} \le \Sigma_i a_i \chi_0^{n_i} \le \Sigma_i a_i \frac{n_i}{n_i^{\max}} \chi_0^{n_i} = -\frac{1}{8n_i^{\max}}, \tag{35}$$

where $n_i^{\max}$ and $n_i^{\min}$ are the maximum and minimum value of n_i. Thus, $\Sigma_i a_i \chi_0^{n_i}$ can be estimated as

$$\Sigma_i a_i \chi_0^{n_i} = -\frac{1}{8\bar{n}}, \tag{36}$$

where $n_i^{\max} \le \bar{n} \le n_i^{\max}$. Furthermore, substituting it into Eq. 34, an asymptotic solution of the liquid front φ_{m} is obtained,

$$\varphi_{\mathrm{m}} = \sqrt{\frac{8\bar{n}}{\bar{n}-1} r_{\mathrm{w}}^0 t}. \tag{37}$$

It suggests $\varphi_\mathrm{m} \sim t^{1/2}$ which aligns with the liquid imbibition in a capillary tube or a homogeneous porous media described by the Lucas-Washburn equation (Cai et al., 2022). Furthermore, the merging time t_merge, at which two liquid fronts from both sides touch each other can be estimated. Here, we only consider the contribution of the linear term in Eq. 32, and by letting $\varphi_\mathrm{m} = \pi$,

$$t_\mathrm{merge} \approx \frac{\pi^2}{8r_\mathrm{w}^0}. \tag{38}$$

2.3 Numerical solution

We now numerically solve the time-evolution equation Eq. 24 for validating our proposed law $\varphi_\mathrm{m} \sim t^{1/2}$. Besides the boundary condition at the liquid source ($\varphi = 0$), the one at the merging point ($\varphi = \pi$) is set as $r_\mathrm{w}|_{\varphi=\pi} = r_\mathrm{w}^\mathrm{min}$. Then, the capillary pressure is calculated as per Eq. 15,

$$P_\mathrm{c} = \gamma \left(\frac{1}{r_\mathrm{w}^0} - \frac{1}{r_\mathrm{w}^\mathrm{min}} \right) \frac{\cos\theta - \sin\theta}{\bar{k}}. \tag{39}$$

Since the liquid front is regarded as a point, $r_\mathrm{w}^\mathrm{min}$ should be zero. However, the capillary pressure would be an infinite value if $r_\mathrm{w}^\mathrm{min} = 0$ as per Eq. 39, resulting in a convergence issue. Therefore, we take a finitely small value as $r_\mathrm{w}^\mathrm{min}$, and r_w is initialized with $r_\mathrm{w}^\mathrm{min}$, i.e., $r_\mathrm{w}|_{t=0} = r_\mathrm{w}^\mathrm{min}$. The Eq. 24 with the boundary conditions is solved on a domain $\varphi \in [0, \pi]$ using the finite element method.

We first investigate the effect of $r_\mathrm{w}^\mathrm{min}$. As shown in figure 2, cases with $r_\mathrm{w}^\mathrm{min}$ ranging from 3e−5 to 1e−3 are almost overlapped regarding the time evolution of the liquid front position in figure 2(a) and the r_w profiles in figure 2(b). A difference is observed in the zoom-in plot around the liquid front in figure 2(b), suggesting that the value of $r_\mathrm{w}^\mathrm{min}$ only influences the local region in the vicinity of the liquid front. More importantly, the measured log-log slope of curves φ_m vs. t, as shown in figure 2(a), confirms $\varphi_\mathrm{m} \sim t^{1/2}$ at late times.

Another scaling law that $\varphi_\mathrm{m} \sim \sqrt{r_\mathrm{w}^0}$, suggested by Eq. 37, is rationalized and verified. From Eq.39, it suggests that the larger r_w^0 is, the stronger P_c is and thus the faster the wetting film spreads along the corner. Furthermore, as shown in figure 3(a), cases with various r_w^0 ranging from 0.03 to 0.12 collapsed as one line on the $\varphi_\mathrm{m}/\sqrt{r_\mathrm{w}^0}$-$t$ space. In addition, the merging time t_merge for each case is directly measured from the numerical result and compared against the theoretical estimation from Eq. 38. Figure 3(b) shows that both numerical solutions and theoretical estimations have the same trend, but Eq. 38 underestimates t_merge as per the comparison. This inconsistency should be attributed to the transition period at the early time, as can be seen in figure 3(a). During the transition period, the interfacial profile is relaxed and self-adjusted to progressively follow the law $\varphi_\mathrm{m} \sim t^{1/2}$. Nevertheless, predicting the transition period is out of the scope of the theoretical model.

3 Volume-of-Fluid simulation

Given that our theoretical model is developed on the foundational assumption of the "arc-shape interface", it is necessary to gauge the practical applicability of our theoretical model and further test the proposed scaling law. In this section, we will conduct numerical simulations using the Volume-of-Fluid (VoF) method. Not only for the verification, we also investigate the film wrapping problems under diverse conditions.

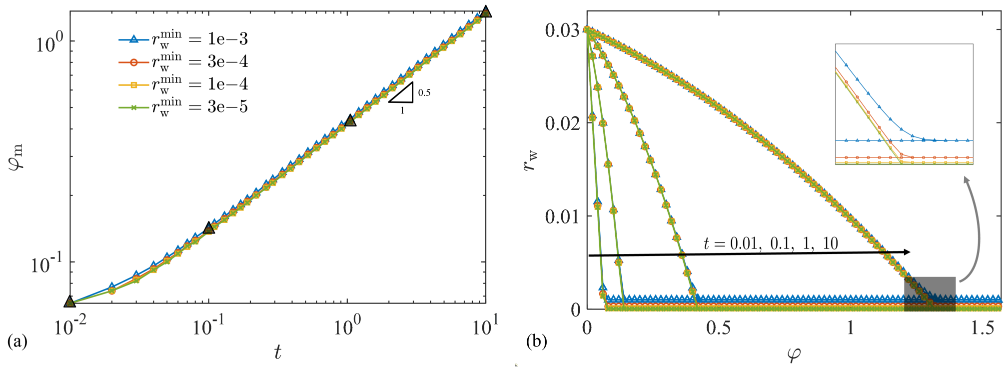

Figure 2. (a) The evolution of φ_{m} of cases with $r_{\mathrm{w}}^0 = 0.03$ and various $r_{\mathrm{w}}^{\mathrm{min}} \in [1\mathrm{e}{-3}, 3\mathrm{e}{-4}, 1\mathrm{e}{-4}, 3\mathrm{e}{-5}]$. (b) The corresponding r_{w} profiles at different times which are marked by black triangles in (a), and the insert is a zoom-in plot of liquid fronts.

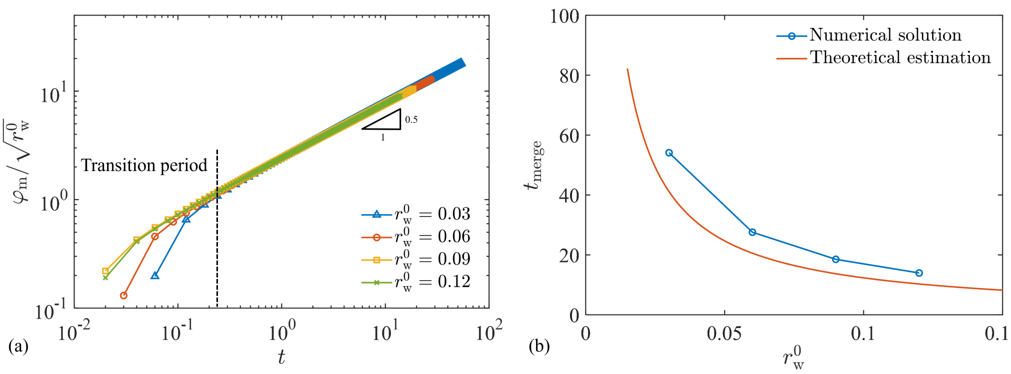

Figure 3. (a) The evolution of scaled φ_{m} of cases with $r_{\mathrm{w}}^{\mathrm{min}} = 3\mathrm{e} - 4$ and various $r_{\mathrm{w}}^0 \in [0.03, 0.06, 0.09, 0.12]$. (b) The comparison of t_{merge} obtained from the numerical solution and theoretical estimation (Eq. 38) under various r_{w}^0.

3.1 Governing equations

We consider the imbibition as a laminar, incompressible, and immiscible two-phase flow, which is governed by the Navier-Stokes equations,

$$\nabla \cdot \boldsymbol{v} = 0, \tag{40}$$
$$\rho \partial \boldsymbol{v}/\partial t + \rho \nabla \cdot (\boldsymbol{v}\boldsymbol{v}) = -\nabla p + \mu \nabla^2 \boldsymbol{v} + \boldsymbol{F}_\gamma, \tag{41}$$

where $\boldsymbol{v}$ denotes the velocity vector; p, ρ, μ are respectively the fluid pressure, density and viscosity; $\boldsymbol{F}_\gamma$ is the surface tension force per unit volume. The interface between two phases is tracked by the volume-of-fluid (Vof) method, wherein a scalar transport equation regarding volume fraction α is introduced,

$$\partial \alpha/\partial t + \nabla \cdot (\boldsymbol{v}\alpha) = 0. \tag{42}$$

The interface is reconstructed based on α-field and related geometric features including interface normal $\boldsymbol{n}_\alpha$ and curvature κ are obtained. Then, $\boldsymbol{F}_\gamma$ is calculated as (Brackbill et al., 1992)

$$\boldsymbol{F}_\gamma = \gamma \kappa \nabla \alpha, \tag{43}$$

Wetting conditions are implemented by correcting the $\boldsymbol{n}_\alpha$ in the vicinity of the solid walls (Saha & Mitra, 2009),

$$\boldsymbol{n}_\alpha = \boldsymbol{n}_s \cos\theta + \boldsymbol{t}_s \sin\theta, \tag{44}$$

where $\boldsymbol{n}_s$ and $\boldsymbol{t}_s$ are the unit normal and tangent vectors to solid walls, respectively. Eq. 40-42 with the following boundary conditions are solved using OpenFOAM (Roenby et al., 2016; Scheufler & Roenby, 2019).

3.2 Numerical model

We build up a three-dimensional numerical model, as shown in figure 4(a). Considering this problem is a symmetric one, a half-cylinder zone is adopted as the computation domain. The symmetry plane, as marked by dash-dot lines in figure 4(b), is divided by the cylinder wall into two face boundaries, i.e., the left and right face. At the right face, where the liquid fronts from both sides will touch, symmetric boundary conditions are imposed for the flow field and the α field. At the left face, we control the α field to simulate different types of the liquid source, including the "fixed boundary" mimicking the situation where r_w is fixed at the liquid source and the "free boundary" where r_w can freely grow at the liquid source as described in detail in the following. Wetting wall boundary conditions are set on the cylinder wall and the bottom wall, as marked in figure 4(a), following Eq. 44. Other boundaries connect to the environment and thus a zero-pressure condition and a zero-gradient α field are imposed.

The radius of the domain is $3R_0$ and its height is $2R_0$. The upper limit of mesh size is set as $R_0/100$, which has passed the mesh-sensitive test. We set the viscosity ratio as 100 which is large enough to represent a gas-liquid situation. The quantities including r_w, h_w, φ_m are directly measured from the reconstructed interface. For the convenience of comparing with the theoretical model, all lengths and times presented in the following have been scaled by R_0 and t^* separately.

3.2.1 *Fixed boundary*

We firstly simulate the situation with fixed α field at the left face, which is expected to agree with the theoretical predictions in Section 2.2. Specifically, provided r_w^0 and θ, the interface position at the left face is calculated as per Eq. 1, and then the liquid and gas phase separated by the interface are mapped on the α field at the left face.

We conduct simulations over a range of $r_\mathrm{w}^0 \in [0.3, 0.5]$ and $\theta \in [15°, 20°, 25°, 30°]$. Figure 5(a) shows the evolution of φ_m scaled by $\sqrt{r_\mathrm{w}^0}$ in the log-log space. For the group

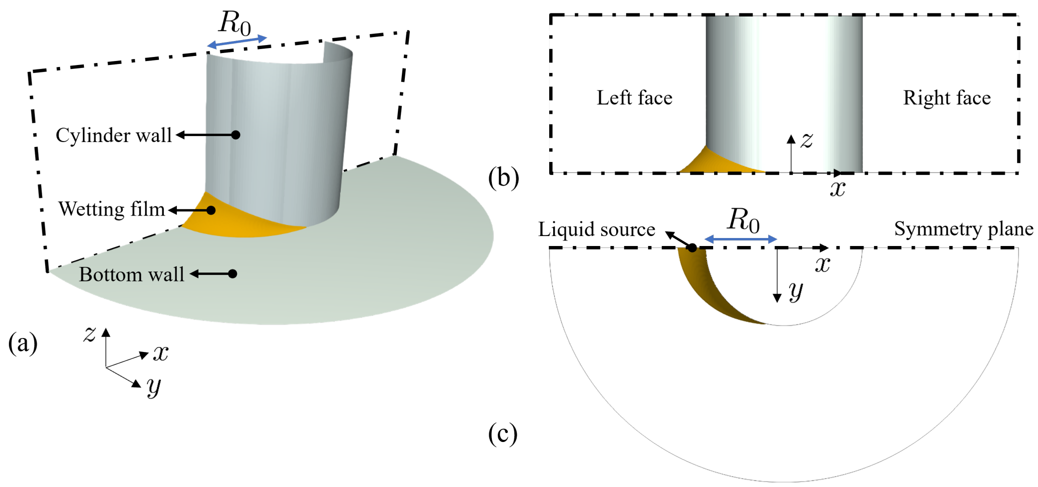

Figure 4. Geometrical settings of the numerical model in a perspective (a), front (b), and top view (c).

of cases with the same r_{w}^0, simulation results from various-θ cases are overlapped, suggesting that the effect of wettability is well considered in t^*. Moreover, the scaling law $\varphi_{\mathrm{m}} \sim \sqrt{r_{\mathrm{w}}^0}$ is also verified to a good extent, since the two groups are significantly close to each other and almost collapse as one line, though a small gap is observed. To better provide insights into the evolution of φ_{m}, we calculate the secant slopes of φ_{m}-t curves in the log-log space, as defined as

$$\frac{\Delta \log \varphi_{\mathrm{m}}}{\Delta \log t} = \frac{\log \frac{\varphi_{\mathrm{m}}(t+\mathrm{d}t)}{\varphi_{\mathrm{m}}(t-\mathrm{d}t)}}{\log \frac{t+\mathrm{d}t}{t-\mathrm{d}t}}, \tag{45}$$

where $\mathrm{d}t$ is the scaled time interval. As shown in figure 5(b), each case has a transition period at the early time, during which the secant slope sharply decreases from a large value and then becomes flattened. The length of such a transition period depends on r_{w}^0 and θ, but it generally takes around $2t^*$ before the evolution reaches the steady state. The steady slope, though floating over a range of $[0.47, 0.55]$, is close to 0.5, indicating that the proposed law $\varphi_{\mathrm{m}} \sim t^{1/2}$ effectively governs the imbibition dynamics. Besides, t_{merge} measured from simulation results is compared with the theoretical estimation from Eq. 38, as presented in figure 5(c). The scaled t_{merge} seems a function of θ, while it should be independent of θ according to the theoretical model where the impacts of θ have been considered in t^*. This is owing to the transition period which is θ-dependent and involved in the measured t_{merge}. Although deviations between predicted and measured t_{merge} are observed, the theoretical model provides a reasonable lower-bound estimation of t_{merge}.

What's more, to further confirm the practicability of our theoretical model, we test the foundational assumption that the interface on the r-z plane maintains arc-shape. Figure 5(d) shows the evolution of h_{w}-r_{w} at $\varphi = \pi/2$ of each case. With imbibition ongoing, the wetting film expands within the r-z plane and h_{w} should increase at the same rate with r_{w} as per the assumption, i.e., $r_{\mathrm{w}} = h_{\mathrm{w}}$ as marked by the dashed line in figure 5(d). It is observed that the measured r_{w}-h_{w} aligns well with the assumption, especially at the early time when r_{w} is small. With r_{w} increasing, though a slight deviation occurs, i.e., h_{w} becomes smaller than r_{w}, the assumption is still acceptable. Noteworthily, this deviation is only determined by the relative size of the wetting film to the cylinder radius. In our theoretical model, only the curvature within the r-z plane is considered for calculating the capillary pressure. However, with the wetting film expanding and r_{w} increasing to close to 1, the contribution of the other principle curvature to

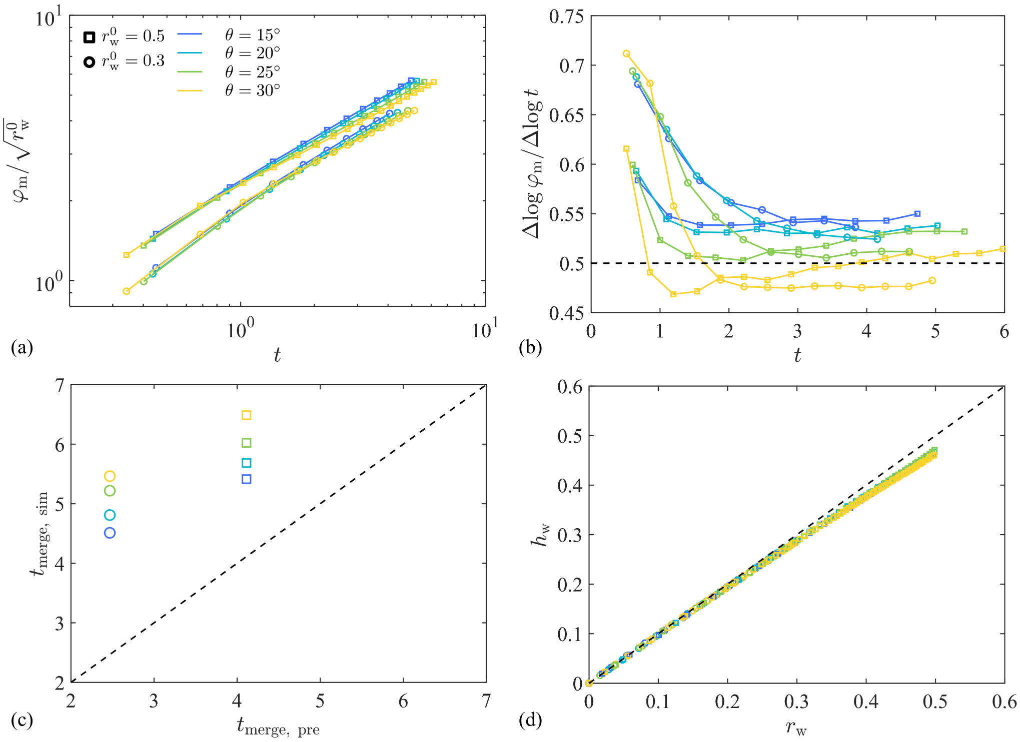

Figure 5. Simulation results of the fixed-boundary situation with $r_w^0 \in [0.3, 0.5]$ and $\theta \in [15°, 20°, 25°, 30°]$. The evolution of (a) the scaled φ_m and (b) the corresponding secant slope. (c) The comparison of t_{merge} against the theoretical prediction. (d) The wetting height h_w vs. the wetting width r_w at $\varphi = \pi/2$.

the capillary pressure may not be neglected. Thus, the effective scope of our theoretical model should be limited to the "small-film-size" regime. Additionally, the deviation from the "arc-shape interface" assumption could be another source of the failure in precisely predicting t_{merge}.

3.2.2 Free boundary

We then extend our focus to another situation where the size of the wetting film at the liquid source can freely grow. Correspondingly, the zero-gradient boundary condition for α field is imposed at the left face.

The simulation cases cover various $\theta \in [15°, 20°, 25°, 30°]$. Initially, a small arc-shape patch (around $0.05R_0$) is set as a liquid phase at the corner of the left face. It relaxes and evolves to form a meniscus after one recording time step dt. We regard the size of such formed meniscus as a initial value r_w^0 at the liquid source, which depends on θ, as shown in figure 6(a). However, since growth curves under various θ are observed paralleled, the growths of r_w at the liquid source are in a similar track, approximately following a power law. The average power is measured as 0.23, which is marked in figure 6(b). Equivalently, as for the theoretical model, the boundary at the liquid source $r_w|_{\varphi=0}$ is time-dependent, i.e.,

$$r_w|_{\varphi=0} \approx r_w^0 t^{0.23}. \tag{46}$$

The analysis in Section 2.2 maintains effective but an adaption is needed. Considering the transient formation of $r_\mathrm{w}|_{\varphi=0}$, Eq. 37 is modified as

$$\varphi_\mathrm{m} \approx \sqrt{\frac{8\bar{n}}{\bar{n}-1} r_\mathrm{w}^0 t^{1.23}}. \tag{47}$$

Thus, we obtain an approximate scaling law $\varphi_\mathrm{m} \sim t^{0.615}$ adapted to the free-boundary situation. The liquid front position is measured from our simulation results, and its evolution and secant slopes are demonstrated in figure 6(c) and (d). Similarly, after a transition period, liquid front advancing reaches a steady state. The steady slope of each case tends to be around 0.6, as marked in figure 6(d), which is comparable to the theoretically predicted value 0.615. Moreover, based on the Eq. 47, we can estimate t_merge as

$$t_\mathrm{merge} \approx \left(\frac{\pi^2}{8 r_\mathrm{w}^0}\right)^{\frac{1}{1.23}}. \tag{48}$$

This estimation still serves as a lower bound of t_merge, as observed in figure 6(e). Again, we test the foundational assumption of the "arc-shape interface" in the free-boundary situation using h_w-r_w on the $\varphi = \pi/2$ plane. As shown in figure 6(f), the deviation is linearly enlarged with r_w, and the relative error $(r_\mathrm{w} - h_\mathrm{w})/r_\mathrm{w}$ is larger than 10% when $r_\mathrm{w} = 0.8$, probably suggesting that the contribution of the secondary principle curvature has to be considered if r_w further increases.

We now shift our focus to imbibition dynamics after merging. Though post-merging behaviours are beyond the scope of the theoretical model, our simulation results provide insights into them. After the two fronts merge at the right face, the film continues to expand in the free-boundary situation. We show the evolution of r_w at the right face in figure 7(a) and the secant slopes in figure 7(b). The expanding rate of r_w decreases at the beginning and gradually tends to be a constant value, i.e., 1.11 as marked in figure 7(b). In another word, r_w increases with time approximately in a linear mode, which is significantly faster compared to the one at the liquid source, see figure 6(b).

4 Conclusion

In this work, We have theoretically and numerically investigated the spontaneous imbibition of a liquid wetting a cylinder corner. Using the Onsager variational principle, a time evolution equation for the meniscus profile was built up. Based on the time evolution equation, we derived an asymptotic solution of the liquid front $\varphi_\mathrm{m} \sim \sqrt{r_\mathrm{w}^0 t}$. It suggests that the advance of the liquid front follows the Lucas-Washburn kinetics, i.e., the $t^{1/2}$ scaling, if the boundary r_w^0 is time-independent; otherwise, the effect of the dynamic boundary should be included and the scaling accordingly changes. Then, the imbibition process was numerically simulated using VoF method, and the simulation results can be well rationalized by our proposed scaling law to a large extent. Furthermore, we provide a theoretical prediction of t_merge, which is demonstrated as a lower bound of the real one.

Our theoretical model is extensible. More complex geometries, such as tapered, ellipse, or even any arbitrary-shape symmetric cylinders, can be modelled by modifying the expression of the free energy. We can expect the scaling coefficient C and characteristic time t^* varies with the geometry while the scaling $t^{1/2}$ maintains effective. Moreover, another demanding aspect for future works is to investigate the imbibtion flows in a cylinder group, and model how the liquid front spreads among neighboring cylinders.

Appendix A Determination of $\bar{k}(\theta)$

We determine the relative permeability $\bar{k}(\theta)$ using numerical experiments. Eq. 16 is solved on a axisymmetric meniscus domain, as shown in figure A1, whose geometry

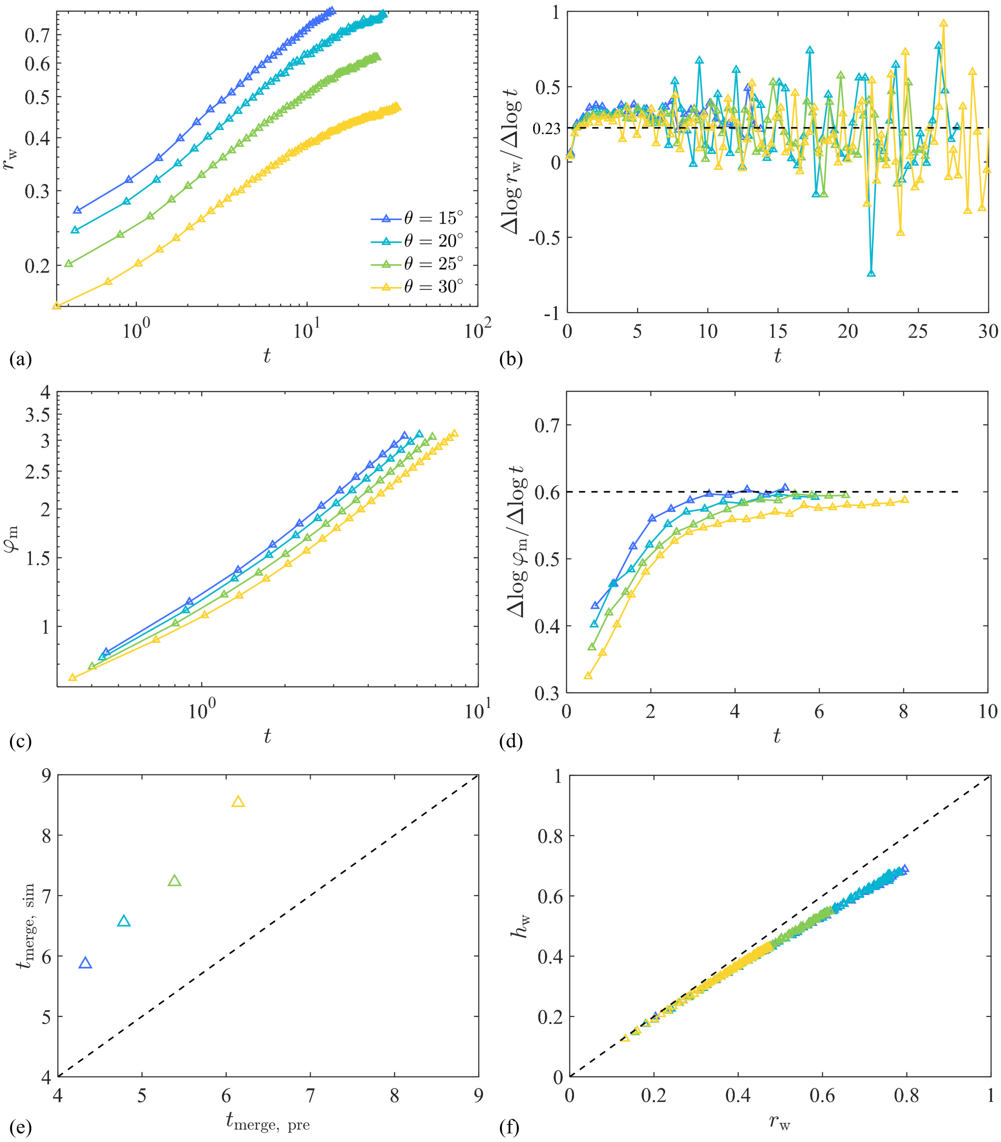

Figure 6. Simulation results of the free-boundary situation with $\theta \in [15^\circ, 20^\circ, 25^\circ, 30^\circ]$. The evolution of (a) r_w at the liquid source and (b) the corresponding secant slope. The evolution of (c) φ_m and (d) the corresponding secant slope. (e) The comparison of t_merge against the theoretical prediction. (f) The wetting height h_w vs. the wetting width r_w at $\varphi = \pi/2$.

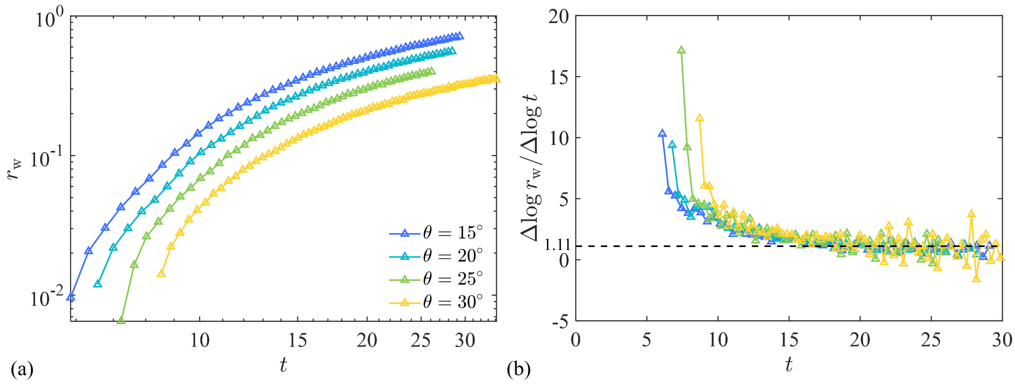

Figure 7. The post-merging dynamics of the free-boundary situation including (a) the evolution of rw at the right face and (b) the corresponding secant slope.

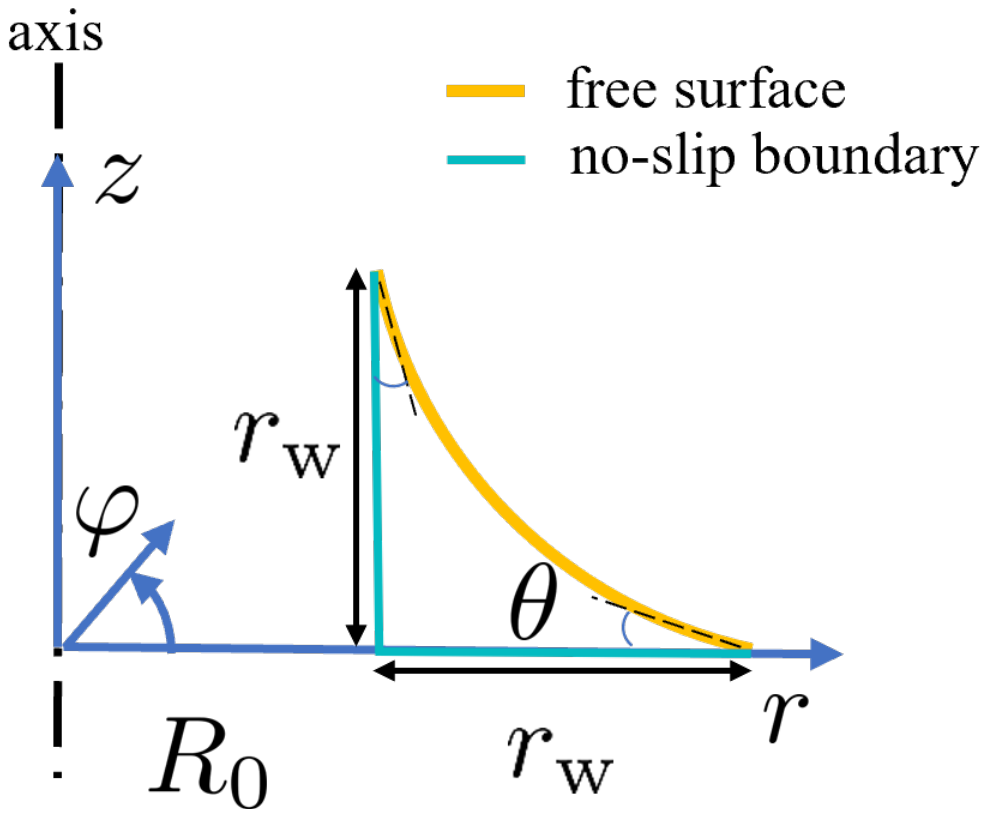

Figure A1. The computation model for determining the relative permeability $\bar{k}(\theta)$

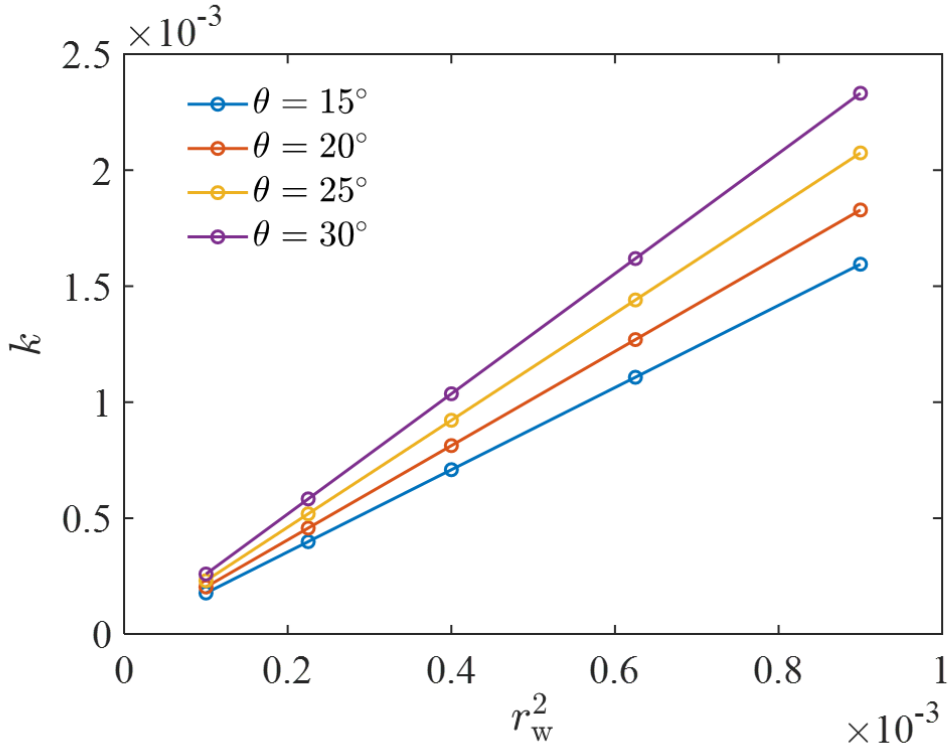

Figure A2. The permeability k vs. r_{w}^2 for various θ.

Table A1. Relative permeability $\bar{k}(\theta)$

15°	20°	25°	30°
0.01772	0.02032	0.02305	0.02591

is dependent on θ and r_{w}. We sweep the parameter combinations of $\theta \in [15°, 20°, 25°, 30°]$ and $r_{\mathrm{w}} \in [0.10, 0.15, 0.20, 0.25, 0.30]$, and calculate the permeability k according to Eq. 18. Figure A2 shows that the permeability k is proportional to r_{w}^2 for any θ. Thus, the relative permeability $\bar{k}(\theta)$ can be obtained by measuring the slope of k-r_{w}^2 lines, which are summarized in table A1.

Acknowledgments

References

Brackbill, J. U., Kothe, D. B., & Zemach, C. (1992). A continuum method for modeling surface tension. *Journal of computational physics*, *100*(2), 335–354.

Cai, J., Chen, Y., Liu, Y., Li, S., & Sun, C. (2022). Capillary imbibition and flow of wetting liquid in irregular capillaries: A 100-year review. *Advances in Colloid and Interface Science*, *304*, 102654.

Cai, J., Jin, T., Kou, J., Zou, S., Xiao, J., & Meng, Q. (2021). Lucas–washburn equation-based modeling of capillary-driven flow in porous systems. *Langmuir*, *37*(5), 1623–1636.

Concus, P., & Finn, R. (1969). On the behavior of a capillary surface in a wedge.

Proceedings of the National Academy of Sciences, *63*(2), 292–299.
Cox, S., Davarpanah, A., & Rossen, W. (2023). Interface shapes in microfluidic porous media: conditions allowing steady, simultaneous two-phase flow. *Transport in Porous Media*, *147*(1), 197–216.
Deng, D., Tang, Y., Zeng, J., Yang, S., & Shao, H. (2014). Characterization of capillary rise dynamics in parallel micro v-grooves. *International Journal of Heat and Mass Transfer*, *77*, 311–320.
Doi, M. (2013). *Soft matter physics.* Oxford University Press, USA.
Gurumurthy, V. T., Rettenmaier, D., Roisman, I. V., Tropea, C., & Garoff, S. (2018). Computations of spontaneous rise of a rivulet in a corner of a vertical square capillary. *Colloids and Surfaces A: Physicochemical and Engineering Aspects*, *544*, 118–126.
Ha, J., Kim, J., Jung, Y., Yun, G., Kim, D.-N., & Kim, H.-Y. (2018). Poro-elasto-capillary wicking of cellulose sponges. *Science advances*, *4*(3), eaao7051.
Higuera, F., Medina, A., & Linan, A. (2008). Capillary rise of a liquid between two vertical plates making a small angle. *Physics of Fluids*, *20*(10).
Hu, R., Wan, J., Yang, Z., Chen, Y.-F., & Tokunaga, T. (2018). Wettability and flow rate impacts on immiscible displacement: A theoretical model. *Geophysical Research Letters*, *45*(7), 3077–3086.
Primkulov, B. K., Pahlavan, A. A., Fu, X., Zhao, B., MacMinn, C. W., & Juanes, R. (2021). Wettability and lenormand's diagram. *Journal of Fluid Mechanics*, *923*, A34.
Roenby, J., Bredmose, H., & Jasak, H. (2016). A computational method for sharp interface advection. *Royal Society open science*, *3*(11), 160405.
Rye, R., Yost, F., & Mann, J. (1996). Wetting kinetics in surface capillary grooves. *Langmuir*, *12*(20), 4625–4627.
Saha, A. A., & Mitra, S. K. (2009). Effect of dynamic contact angle in a volume of fluid (vof) model for a microfluidic capillary flow. *Journal of colloid and interface science*, *339*(2), 461–480.
Scheufler, H., & Roenby, J. (2019). Accurate and efficient surface reconstruction from volume fraction data on general meshes. *Journal of computational physics*, *383*, 1–23.
Suo, S., Liu, M., & Gan, Y. (2019). Modelling imbibition processes in heterogeneous porous media. *Transport in Porous Media*, *126*, 615–631.
Tang, L.-H., & Tang, Y. (1994). Capillary rise in tubes with sharp grooves. *Journal de Physique II*, *4*(5), 881–890.
Washburn, E. W. (1921). The dynamics of capillary flow. *Physical review*, *17*(3), 273.
Weislogel, M. M. (2012). Compound capillary rise. *Journal of Fluid Mechanics*, *709*, 622–647.
Yu, T., Zhou, J., & Doi, M. (2018). Capillary imbibition in a square tube. *Soft Matter*, *14*(45), 9263–9270.
Zhao, B., MacMinn, C. W., & Juanes, R. (2016). Wettability control on multiphase flow in patterned microfluidics. *Proceedings of the National Academy of Sciences*, *113*(37), 10251–10256.
Zhao, B., MacMinn, C. W., Primkulov, B. K., Chen, Y., Valocchi, A. J., Zhao, J., … others (2019). Comprehensive comparison of pore-scale models for multiphase flow in porous media. *Proceedings of the National Academy of Sciences*, *116*(28), 13799–13806.
Zhao, J., Qin, F., Fischer, R., Kang, Q., Derome, D., & Carmeliet, J. (2021). Spontaneous imbibition in a square tube with corner films: theoretical model and numerical simulation. *Water Resources Research*, *57*(2), e2020WR029190.
Zhou, J., & Doi, M. (2020). Universality of capillary rising in corners. *Journal of Fluid Mechanics*, *900*, A29.